Journal of Astronomical Telescopes, Instruments, and Systems

AstronomicalTelescopes.SPIEDigitalLibrary.org

Low-order wavefront sensing and control for WFIRST-AFTA coronagraph

Fang Shi
Kunjithapatham Balasubramanian
Randall Hein
Raymond Lam
Douglas Moore
James Moore
Keith Patterson
Ilya Poberezhskiy
Joel Shields
Erkin Sidick
Hong Tang
Tuan Truong
J. Kent Wallace
Xu Wang
Daniel Wilson

SPIE.

Fang Shi, Kunjithapatham Balasubramanian, Randall Hein, Raymond Lam, Douglas Moore, James Moore, Keith Patterson, Ilya Poberezhskiy, Joel Shields, Erkin Sidick, Hong Tang, Tuan Truong, J. Kent Wallace, Xu Wang, Daniel Wilson, "Low-order wavefront sensing and control for WFIRST-AFTA coronagraph," *J. Astron. Telesc. Instrum. Syst.* **2**(1), 011021 (2016), doi: 10.1117/1.JATIS.2.1.011021.

Low-order wavefront sensing and control for WFIRST-AFTA coronagraph

Fang Shi,* Kunjithapatham Balasubramanian, Randall Hein, Raymond Lam, Douglas Moore, James Moore, Keith Patterson, Ilya Poberezhskiy, Joel Shields, Erkin Sidick, Hong Tang, Tuan Truong, J. Kent Wallace, Xu Wang, and Daniel Wilson
Jet Propulsion Laboratory, California Institute of Technology, 4800 Oak Grove Drive, Pasadena, California 91009, United States

Abstract. To maintain the required Wide-Field Infrared Survey Telescope (WFIRST) coronagraph performance in a realistic space environment, a low-order wavefront sensing and control (LOWFS/C) subsystem is necessary. The LOWFS/C uses the rejected stellar light from the coronagraph to sense and suppress the telescope pointing errors as well as low-order wavefront errors (WFEs) due to changes in thermal loading of the telescope and the rest of the observatory. We will present a conceptual design of a LOWFS/C subsystem for the WFIRST-AFTA coronagraph. This LOWFS/C uses a Zernike phase contrast wavefront sensor (ZWFS) with a phase shifting disk combined with the stellar light rejecting occulting masks, a key concept to minimize the noncommon path error. We will present our analysis of the sensor performance and evaluate the performance of the line-of-sight jitter suppression loop, as well as the low-order WFE correction loop with a deformable mirror on the coronagraph. We will also report the LOWFS/C testbed design and the preliminary in-air test results, which show a very promising performance of the ZWFS. [DOI: 10.1117/1.JATIS.2.1.011021]

Keywords: wavefront sensing and control; stellar coronagraph; Wide-Field Infrared Survey Telescope.

Paper 15049SS received Jun. 13, 2015; accepted for publication Feb. 11, 2016; published online Mar. 15, 2016.

1 Introduction

The Wide-Field Infrared Survey Telescope (WFIRST) was the top-ranked large space mission in the New Worlds New Horizons Decadal Survey of Astronomy and Astrophysics in 2010.[1] When the two existing 2.4-m diameter telescopes known as the Astrophysics Focused Telescope Assets (AFTA) were made available to NASA, one of them was directed for the updated WFIRST-AFTA mission concept. Later in 2013, a coronagraph instrument (CGI) was added to the payload as the second instrument. The WFIRST-AFTA coronagraph will be the first active, high-contrast stellar coronagraph in space intended for imaging, discovery, and spectral characterization of Jupiter, Neptune, and possibly super-Earth sized exoplanets, as well as debris discs.

To minimize potential mission cost growth, the coronagraph was added to the payload under the condition that it does not drive the telescope and spacecraft requirements. This constraint has guided the technical decisions made by the coronagraph design and technology development teams, who have made great efforts to work with the telescope and observatory as is and either adapt to the existing capabilities or compensate for them inside the CGI. Since the bulk of the coronagraph technology development work prior to WFIRST-AFTA was done for unobscured pupil telescopes,[2] WFIRST-AFTA telescope pupil obscurations consisting of the secondary mirror and its supporting struts presented the initial challenge to the coronagraph design teams. However, the selected designs are all capable of producing high contrast in a small inner-working angle in the presence of the WFIRST-AFTA pupil, and such capabilities have since been validated experimentally in coronagraph testbeds.

The other challenge of the WFIRST observatory is the optical wavefront stability necessary to achieve the required level of starlight suppression and the stability of coronagraph contrast. The wavefront dynamics presented to the coronagraph can be decomposed into the following components:

- Slow line-of-sight (LoS) pointing errors at frequencies below 2 Hz due to the error of the observatory's attitude control system (ACS).
- Fast LoS pointing jitter at frequencies above 2 Hz due to structural resonance modes excited by the four reaction wheels (RWs) used for observatory's ACS
- Slow low-order wavefront (LOWF) errors at frequencies below 2 Hz that are largely caused by the sunshine and Earth shine driven thermal changes on the telescope optics and structure.
- Fast LOWF jitter above 2 Hz that is caused by vibration of optics excited mainly by the RWs.

The approach taken to mitigate the impact of these optical wavefront disturbances is threefold:

1. Minimizing wavefront dynamics at the telescope and spacecraft level. Appropriate telescope thermal shielding, isolation of the RWs, and good structural design of the observatory are done to the level that is consistent with the mission budget and sufficient to meet the requirements of the wide-field infrared instrument. These observatory level decisions and improvements are not driven by the coronagraph needs.
2. Selection of the coronagraph designs that have acceptably low sensitivity to wavefront errors (WFEs). These sensitivities are a key part of each coronagraph's

*Address all correspondence to: Fang Shi, E-mail: Fang.Shi@jpl.nasa.gov

2329-4124/2016/$25.00 © 2016 SPIE

design evaluation. As the coronagraph designs are evolved, a trend toward producing better science in the presence of realistic wavefront dynamics is evident.

3. Measurement and suppression of the WFEs presented to the coronagraph in order to (a) reduce them and (b) use their knowledge in data postprocessing to separate residual starlight speckles from the planet light.

The last of these mitigations is the subject of this paper, which describes the WFIRST-AFTA low-order wavefront sensing and control (LOWFS/C) subsystem. This subsystem has been developed to work for the primary WFIRST coronagraph architecture called the occulting mask coronagraph (OMC) that combines two operating modes: shaped pupil coronagraph (SPC) and hybrid Lyot coronagraph (HLC). These two modes share the same LOWFS/C hardware. The backup architecture called phased-induced amplitude apodization complex mask coronagraph (PIAACMC) also has a viable LOWFS/C design, but is not discussed in this paper.

The development and demonstration of LOWFS/C subsystem for OMC is an important part of the technology development program approved by NASA to mature the coronagraph to Technology Readiness Level (TRL) 5. A stand-alone wavefront sensing and LoS jitter suppression demonstration is a part of WFIRST coronagraph milestone 6. The work performed since the beginning of 2014 toward this milestone is described in this paper. After the stand-alone LOWFS/C demonstration on the dedicated LOWFS/C testbed, the subsystem will be integrated with the OMC testbed to accomplish a full system demonstration of starlight suppression in the presence of the realistic wavefront disturbances expected in space.

This paper is structured as follows. The current understanding of the optical wavefront disturbances the WFIRST coronagraph will encounter in space is described in Sec. 2. These are the inputs that the coronagraph LOWFS/C must sense and suppress. In Sec. 3, we provide an overview of two LOWFS/C concepts we have evaluated and the results of the trade studies are presented. Section 3 also describes in more detail the concept, and the design of the Zernike wavefront sensor (WFS). Section 4 covers the detailed performance modeling for both HLC and SPC coronagraph operating modes. In this section, we will also describe the LoS control using a fast steering mirror (FSM) and the low-order WFE correction using a deformable mirror (DM). Section 5 presents the LOWFSC testbed design for the planned in-vacuum performance test, and some preliminary results. We conclude this paper in Sec. 6.

2 WFIRST-AFTA Environment and Coronagraph Requirements

As a part of WFIRST-AFTA mission design, high-fidelity structural and thermal models are being developed to understand the dynamics and thermal behavior of the telescope, the instrument carrier, and the CGI in the space environment.[3–5] These increasingly sophisticated models include all WFIRST-AFTA components, from the observatory structure to telescope mirrors to instrument optics. Exercising these models under the currently envisioned coronagraph observation scenarios can predict realistic optical wavefront disturbances, which the CGI will experience during its operation. We use these modeled wavefront disturbances to evaluate their impact on coronagraph performance and to design the LOWFS/C to suppress them so that the coronagraph is able to meet its science requirements.

The primary source of the dynamic disturbance is the RWs used by the WFIRST telescope's ACS. The residual unbalanced momentum and forces from the RWs shake the telescope optics, which causes optical LoS jitter and wavefront jitter. Figure 1 shows the LoS jitter predicted at the first focus of the coronagraph[3,5] from the worst impact wheel. The plot shows the total LoS jitter against wheel speed. At each wheel speed, the jitter contains multiple harmonic frequencies besides the fundamental frequency that equals the wheel speed. In addition to the high-frequency LoS jitter from the RWs, the telescope also suffers a slow (<2 Hz) LoS pointing wander caused by the telescope ACS pointing error. The ACS design allows the telescope pointing to wander up to 14 mas rms per axis. If left uncorrected, the WFIRST LoS jitter and wander would severely degrade the coronagraph's performance. However, the coronagraph design can be tailored and optimized to tolerate some residual LoS jitter. For HLC, this is done by globally optimizing the design of the occulting spot, DM stroke pattern, and Lyot stop.[6] For WFIRST, the coronagraph is designed to deliver the required science assuming a residual LoS error between 0.4 mas rms per axis (good case) and 1.6 mas (bad case). To meet this requirement, we need to design the LOWFS/C subsystem with sufficient bandwidth and sensor accuracy to suppress the LoS jitter and wander.

During the coronagraph observation, the spacecraft orbiting or telescope pointing change the thermal load from the Sun and the Earth, which in turn causes the telescope optics surface figures and positions to change. This thermally induced optical figure or position change will cause low-order WFE which affects coronagraph performance. Figure 2 shows the model-predicted thermally-induced WFE for a notional coronagraph observation scenario that lasts 56 h.[5] From the plot, we can see that the dominant portions of the WFE are focus, astigmatism, and coma generated due to the telescope optics position shifts from the thermal load variations. Higher aberration modes beyond

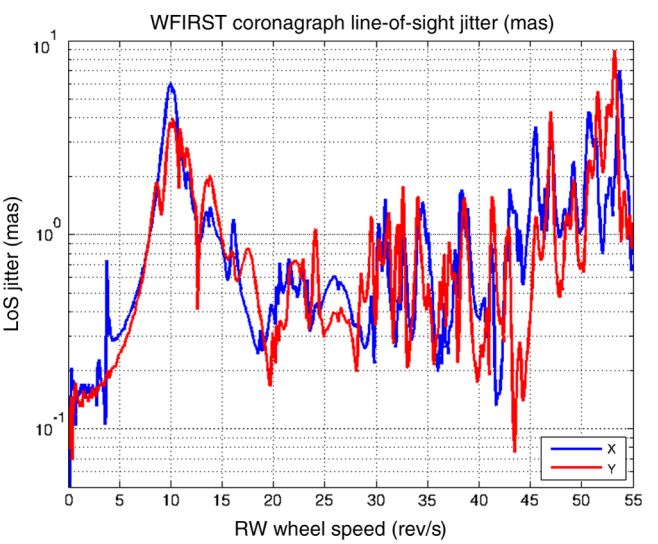

Fig. 1 LoS jitter predicted from the observatory dynamic model and evaluated at the first focus of the WFIRST coronagraph. The *X* and *Y* direction jitters are plotted against the RW speed. During the observation, the RW speed slowly changes between 10 and 40 rev/s over ~18 h.

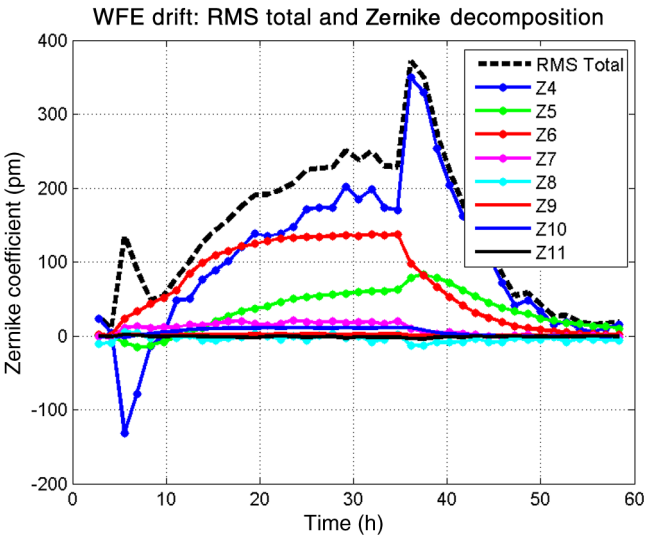

Fig. 2 WFIRST-AFTA thermally induced wavefront error from a typical coronagraph observation scenario. The thermal load variation is from the combination of spacecraft orbiting and change of the telescope pointing during the observation. The black dashed line in the plot is the total WFE from the thermal changes. The colored lines show the decomposed major Zernike components (Z4 to Z11) of the same WFE. Wavefront tilt is not included in the WFE shown here.

spherical are all negligibly small, at the level of single digit picometers. It is also evident that the wavefront wander is very slow compared with LoS jitter, typically under 0.001 Hz.

For most optical systems dynamic WFEs of less than 0.5 nm, RMS is insignificant. However, a high-contrast coronagraph is very sensitive to the wavefront variations. For the WFIRST coronagraph, the science requires[7] the coronagraph to have raw contrast better than 10^{-8}. Furthermore, in order to differentiate planets from residual speckles in the dark hole and to detect a planet with proper signal-to-noise ratio (SNR), the coronagraph contrast needs to be stable at a level on the order of 10^{-10} during the observation. This stability requirement drives a very tight tolerance for the wavefront variation. We can see this from Fig. 3, which shows the coronagraph contrast sensitivities to WFE aberration modes.[5] For example, a 0.1 nm of coma will cause a contrast change of $\sim 10^{-9}$ for the inner working area of the dark hole. The plots also show that the coronagraph contrast sensitivity depends on the OMC instrument operating mode (HLC versus SPC) as well as the wavefront aberration mode, with spherical, coma, and trefoil being the worst offenders. From the WFIRST-AFTA thermal variation (Fig. 2) and WFIRST coronagraph WFE sensitivity (Fig. 3), we can see that in order to achieve the coronagraph stability requirement, the thermally-induced WFE variation needs to be sensed and corrected. In general, the coronagraph contrast scales with WFE squared. That means that the most sensitive modes, such as spherical, coma, and trefoil, need to be stable at a few 10 s of picometer in order to maintain the contrast stability of $\sim 10^{-10}$. These are the wavefront changes that must be measured and corrected by the LOWFS/C subsystem. From the coronagraph performance requirements, the LOWFS/C's sensor is designed to have LoS sensitivity of 0.4 mas and low-order wavefront, focus (Z4) to spherical (Z11), sensitivity on the order of 10 pm. For the WRIST coronagraph, the medium science target magnitude is Mv = 5 with most targets brighter than Mv = 8.[7] These are the stellar magnitudes we evaluate for the LOWFS/C performance.

The WFIRST coronagraph LOWFS/C subsystem works cohesively with the coronagraph's high-order wavefront sensing and control (HOWS/C) subsystem, which is responsible for generating the coronagraph's dark hole using the coronagraph's two 48×48 actuator DMs.[6,8–10] The LOWFS/C does not set the wavefront; instead, it maintains the wavefront set by HOWS/C. In other words, the LOWFS/C is a relative sensing and control system.

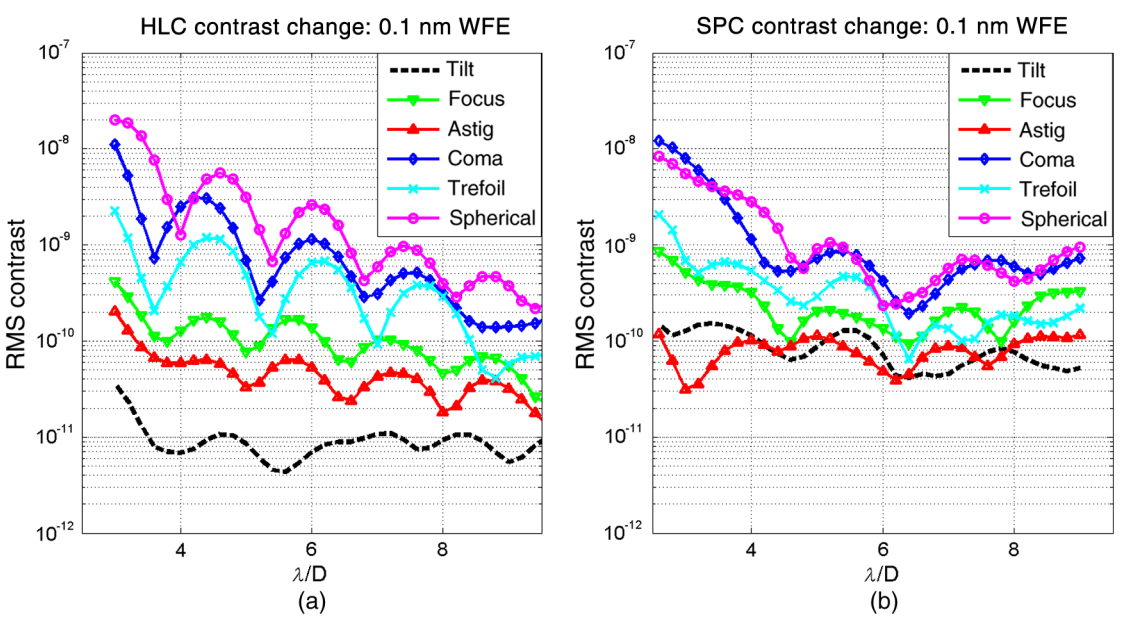

Fig. 3 WFIRST coronagraph contrast sensitivity to different aberration modes. (a) The HLC mode and (b) the SPC mode. The sensitivity curve shows the contrast change as a function of working angle when a 0.1 nm (RMS) of each aberration mode is introduced into the coronagraph.

3 Zernike Wavefront Sensor Concept and its Application to Low-Order Sensing and Control for WFIRST-AFTA

There are many types and various configurations of WFSs, including Shack–Hartmann WFS,[11] pyramid WFS,[12] Mach–Zehnder pupil plane interferometer,[13,14] Zernike (phase-contrast) wavefront sensor (ZWFS),[15] and masked PSF focal plane WFS.[16] In his paper, Guyon[9] has shown a detailed performance comparison of the commonly used WFSs and concludes that the ZWFS and the focal plane WFS are close to being "optimal" WFSs. We note that other types of coronagraphs, which have loss-less focal plane elements (phase-mask coronagraphs such as the four-quadrant phase mask and the vector vortex, for instance) have demonstrated wavefront sensing using light rejected from the Lyot plane.[17] Our baseline coronagraphs, however, are not of this variety. Indeed, both HLC and SPC reject light at the focal. For the HLC, this light particularly needs to be rejected at the focal plane for high-contrast, but is also readily available for wavefront sensing.

During the early stage of LOWFS/C development for the WFIRST coronagraph, we evaluated both the ZWFS and the masked PSF WFS (MPSF-WFS) similar to the one proposed by Guyon[16] as the candidate LOWFS/C sensors. The choice to consider these two candidates was based on the analysis done by Guyon,[9] as well as previous works performed at JPL. The ZWFS concept was proposed by JPL's Bloemhof and Wallace[15] and later more analysis and a practical ZWFS design were done by Wallace et al.[18] A LOWFS/C experiment using MPSF-WFS was carried out at JPL's high-contrast imaging testbed PIAA coronagraph in 2010 which has demonstrated 10^{-3} λ/D LoS control.[19] Also, both types of WFS have the advantage of simple imaging optics and can be combined with the coronagraph's focal plane mask (FPM) to avoid the noncommon path WFE, a key criteria for the WFIRST-AFTA coronagraph LOWFS/C.

For these two sensor candidates, we conducted a trade study which concluded in June of 2014 to analyze and compare their performance in the areas such as sensor linearity and mode cross-talk, sensor noise equivalent angle and sensing error, sensor mask fabrication error tolerance, and the feasibility and complexity of fabrication. The comparisons showed that the performance of these two WFSs was very similar, with both ZWFS and masked-PSF WFS providing good sensitivity and accuracy. However, it was the feasibility of LOWFS/C mask fabrication that turned out to be the main differentiator between the two sensor types. For WFIRST OMC, which includes both HLC and SPC modes, the LOWFS/C sensor uses the rejected starlight reflected by the coronagraph's FPM.[20] To avoid noncommon path errors, it is highly desirable to combine the LOWFS/C sensor mask with the FPM. The ZWFS mask requires depositing a transparent dielectric phase disk of $\sim\lambda/D$ diameter with a thickness that creates $\sim\pi/2$ rad phase difference between the light reflected within the phase disk and light reflected outside. Adding this feature to an SPC FPM that is opaque in the center is not difficult. Moreover, this disc-like feature can be designed and fabricated with the HLC's occulting mask without a negative impact on the HLC starlight suppression performance. On the other hand, the MPSF-WFS mask would require an opaque spot of $\sim\lambda/D$ size in the center of the FPM. Though such a dark spot is compatible with the SPC's bowtie-shaped FPM, designing this opaque spot with a HLC's occulting mask without severely degrading the starlight suppression performance was deemed impractical for the following reason. The HLC FPM consists of a ~ 6 λ/D nickel mask over coated with a spatially patterned dielectric. The nickel is a strong attenuator but is not entirely opaque in transmission, and the leakage from the nickel must be balanced with the judicious design of the dielectric. In reflection off the FPM, the MPSF-WFS would require an additional opaque central spot. This third focal plane element, whose optical properties are unknown, would need to be co-optimized with the nickel and dielectric to achieve optimum contrast. This work might be justified if the performance difference between the MPFS and ZWFS were substantially different enough. In practice, these two methods perform nearly equally. In the end, the ZWFS was baselined for the WFIRST-AFTA coronagraph LOWFS/C due to design and fabrication compatibility with both SPC and HLC occulting masks.

3.1 *Zernike Wavefront Sensor Concept*

The Zernike wavefront sensor is based on the Zernike phase-contrast concept, which was initially proposed by Frits Zernike in the 1930s to enhance the specimen contrast for a microscope by converting a specimen's transparent optical phase variations into intensity variations.[21]

Figure 4 illustrates the concept of the Zernike wavefront sensor in the context of an astronomical instrument. The WFE is represented by the wavefront phase variation at the entrance pupil plane, such as the primary mirror of a telescope. An imaging system (depicted as an imaging lens in the figure) focuses the starlight to form a point source image referred to as the point spread function (PSF) because its intensity distribution contains the imaging system optical properties such as the pupil geometry and WFEs. In this transmissive configuration, a transparent phase disk is placed at the focal plane where the star image is formed, introducing a phase change for the central part of the star image, a region typically $\sim\lambda/D$ in diameter in the PSF space. The light that passes through this small phase disk acts as a reference wavefront (Ref WF in the figure). It interferes with the light passing outside the phase disk which contains the information on wavefront aberrations (Abbr WF in the figure). When the interfered light is reimaged to another pupil, it produces an intensity pattern that is related to the input wavefront aberration (phase error). This intensity pattern can then be detected by a detector such as a CCD camera. The exact intensity encoding of the WFE depends on the phase difference and size of the phase disk, and a quasilinearity is achieved when the phase disk produces a phase difference of about $\pi/2$ rad between the inner and outer parts of the PSF light.

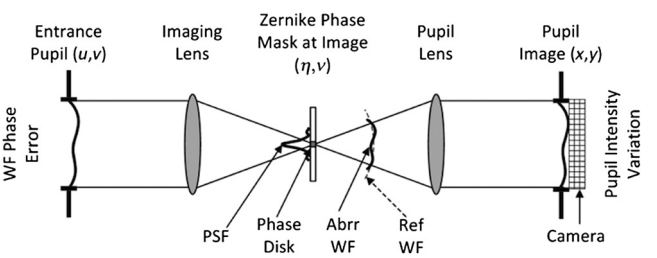

Fig. 4 Illustration of Zernike wavefront sensor concept. Lenses are used to represent the optics between entrance pupil, imaging plane, and reimaged pupil plane. The Cartesian co-ordinates of these planes are also labeled.

The analytical treatment of the Zernike phase contrast wavefront sensing can be found in many optical textbooks.[22,23] In this paper, we follow the treatment used by Wallace et al.[18] Using the simplified concept system and the Cartesian co-ordinates shown in Fig. 4, the electric field at the entrance pupil is given by

$$E(u,v) = P(u,v) \cdot A[1 + \varepsilon(u,v)] \cdot \mathrm{e}^{i\varphi(u,v)}, \tag{1}$$

where $P(u,v)$ is the pupil amplitude support function, which describes the pupil geometry, A is the mean electric field amplitude, $\varepsilon(u,v)$ is the amplitude variation across the entrance pupil, and $\varphi(u,v)$ is the phase variation across the pupil, which is the WFE. The wavefront phase variation $\varphi(u,v)$ is related to the WFE commonly known as optical path difference (OPD) by $\varphi(u,v) = 2\pi/\lambda \ldots \mathrm{OPD}(u,v)$. Assuming that $\varphi(u,v) \ll 1$ rad, the exponential term in Eq. (1) can be expanded into a Taylor series. Ignoring the higher-order terms of $\varphi(u,v)$ and cross terms between $\varepsilon(u,v)$ and $\varphi(u,v)$, the electric field is now given by

$$E(u,v) \approx P(u,v) \cdot A[1 + \varepsilon(u,v) + i\varphi(u,v)]. \tag{2}$$

Imaged by the imaging lens, the electric field at the entrance pupil plane, given by Eq. (2), is propagated to the image plane by a Fourier transform

$$\hat{E}(\eta,\upsilon) = \mathcal{F}[P(u,v)] \ \otimes \ \mathcal{F}\{A[1 + \varepsilon(u,v) + i\varphi(u,v)]\}, \tag{3}$$

where $\mathcal{F}[\cdot]$ represents the Fourier transform operation and the $\otimes$ represents the convolution operation. If the Fourier transform of the pupil function without phase or amplitude error is represented by a complex PSF, denoted here by CPSF, then Eq. (3) becomes

$$\hat{E}(\eta,\upsilon) = A \cdot \mathrm{CPSF}(\eta,\upsilon) + A \cdot \mathrm{CPSF}(\eta,\upsilon) \otimes \mathcal{F}[\varepsilon(u,v) + i\varphi(u,v)]. \tag{4}$$

Equation (4) shows that at the image plane, the electric field $\hat{E}(\eta,\upsilon)$ consists of two components, the first one represents an ideal complex PSF, and the second one contains the amplitude and phase errors. Now, a Zernike phase disk is inserted at the center of the image plane. In the simplified case of Zernike phase disk, which is a uniform phase shift of magnitude θ rad over diameter d, the transmission function $t(\eta,\upsilon)$ can be expressed as

$$t(\eta,\upsilon) = \ 1 - (1 - \mathrm{e}^{i\theta})M, \tag{5}$$

where M is just a top hat function, where $M = 1$ for the area within the phase disk, or radius $\rho = (\eta^2 + \upsilon^2)^{1/2} \le d/2$, and $M = 0$ for the area outside phase disk, or $\rho > d/2$. Since the phase disk is applied to the central core portion of the electric field $\hat{E}(\eta,\upsilon)$, it gives a phase shifted of electric field as

$$\hat{E}(\eta,\upsilon) = A \cdot \mathrm{CPSF}(\eta,\upsilon)\mathrm{e}^{i\theta} + A \cdot \mathrm{CPSF}(\eta,\upsilon) \otimes \mathcal{F}[\varepsilon(u,v) + i\varphi(u,v)]. \tag{6}$$

We should point out that Eq. (6) is simplified in such a way that the phase shift $\mathrm{e}^{i\theta}$ from the phase disk applies only to the ideal complex PSF component. This is because the size of the phase disk is comparable with the CPSF core size where most of the energy of an ideal CPSF is located. Meanwhile, the energy distribution from either the amplitude or phase error component in $\mathcal{F}[\varepsilon(u,v) + i\varphi(u,v)]$ tends to distribute outside the PSF core area, where the phase shift is zero. A more elaborate treatment has been derived by N'Diaye et al.,[24] but when we use the differential image to compute the WFE, as indicated in Eqs. (16) and (17), the subtle difference between these two approaches mostly drops out.

After the Zernike phase disk, the interfered light is reimaged to the second pupil plane. $\hat{E}$ in Eq. (6) is then Fourier transformed again to represent the electric field in the pupil image plane as

$$E(x,y) = P(x,y) \cdot A \cdot [\mathrm{e}^{i\theta} + \varepsilon(x,y) + i\varphi(x,y)]. \tag{7}$$

The reimaged electric field in the output pupil plane represented by Eq. (7) differs from the input pupil plane electric field in Eq. (2), in that the DC part of the electric field has been replaced by a phase-shifted version. Because the remaining expression deals only with the output pupil plane, the explicit pupil notation $P(x,y)$ is dropped hereafter. When the phase shift of the Zernike phase disk $\theta = \pi/2$, the output pupil electric field and intensity are given by

$$\begin{aligned} E(x,y) &= A \cdot \left[\mathrm{e}^{i\frac{\pi}{2}} + \varepsilon(x,y) + i\varphi(x,y)\right] \\ &= A \cdot [i + \varepsilon(x,y) + i\varphi(x,y)], \end{aligned} \tag{8}$$

$$\begin{aligned} I(x,y) &= E(x,y) \cdot E^*(x,y) \\ &= A^2 \cdot [1 + \varepsilon^2(x,y) + 2\varphi(x,y) + \varphi^2(x,y)] \\ &\approx A^2 \cdot [1 + \varepsilon^2(x,y) + 2\varphi(x,y)], \end{aligned} \tag{9}$$

where E^* is the complex conjugate of E field. Equations (8) and (9) show that when phase from the Zernike phase disk is $\pi/2$ rad, the wavefront phase variation at the entrance pupil becomes the linear intensity variation in the ZWFS pupil plane. This is readily measurable with a camera.

To compute the WFE φ from the pupil image intensity, Wallace[18] analytically solved the WFE from Eq. (9). However, Wallace showed that the WFS suffered nonuniform gains across the different Zernike modes and mode cross-talks when using this analytical solution approach.[18]

In WFIRST coronagraph, the role of LOWFS/C is to maintain the wavefront set by the HOWFS/C, which creates the coronagraph's dark hole at the beginning of coronagraphic observation. The WFIRST LOWFS/C's ZWFS, therefore, works in the relative wavefront measurement mode, sensing the wavefront changes from the reference point set by HOWFS/C instead of measuring the absolute wavefront. Because of this and the fact that the wavefront change during the WFIRST coronagraph observation is small, typically less than 1 nm RMS, we construct a differential image-based linear algorithm to compute the relative WFE directly from the pupil image intensity. Continuing from Eq. (9), at the time when coronagraph HOWFS/C has established a dark hole, the LOWFS/C camera takes the reference image denoted as I_{ref}

$$I_{\mathrm{ref}} = A^2 \cdot (1 + \varepsilon_0^2 + 2\varphi_0), \tag{10}$$

where amplitude variation ε_0 and wavefront phase variation φ_0 all have been set by HOWFS/C in the process of creating the coronagraph dark hole which satisfy the condition needed for starlight suppression. The subsequent wavefront change $\Delta\varphi$ causes the pupil image at LOWFS/C camera to be the "aberrated image" I_{abbr}

$$I_{\text{abbr}} = A^2 \cdot [1 + \varepsilon_0^2 + 2(\varphi_0 + \Delta\varphi)]. \tag{11}$$

Then the wavefront change $\Delta\varphi$ is proportional to the image difference of the aberrated image and the reference image ΔI, which can be expressed as

$$\Delta I = I_{\text{abbr}} - I_{\text{ref}} = 2A^2 \cdot \Delta\varphi, \tag{12}$$

and the wavefront phase change is simply related to the differential image ΔI by

$$\Delta\varphi = \left(\frac{I_{\text{abbr}} - I_{\text{ref}}}{2A^2}\right) = \frac{\Delta I}{2A^2}. \tag{13}$$

The WFIRST coronagraph LOWFS/C uses the linearized relationship of differential images and WFE to directly detect WFE. To do that, we first build a WFE to differential image response matrix $\mathbf{K}$. We use the Zernike coefficients to represent the low-order WFE by a vector $\vec{Z}$ where

$$\vec{Z} = \begin{bmatrix} z_2 \\ \vdots \\ z_k \end{bmatrix}. \tag{14}$$

Because WFIRST wavefront variation is mostly low order for WFIRST LOWFS/C, the number of Zernike modes sensed k is typically less than 11 and the first Zernike mode Z1, which is a piston, is not used. We also reorder the two-dimensional differential image ΔI into a vector $\vec{\Delta I}$, as

$$\vec{\Delta I} = \begin{bmatrix} I_{1,1} & \cdots & I_{1,n} \\ \vdots & \ddots & \vdots \\ I_{n,1} & \cdots & I_{n,n} \end{bmatrix} \leftrightarrow \begin{bmatrix} I_{1,1} \\ \vdots \\ I_{n,1} \\ I_{2,1} \\ \vdots \\ \vdots \\ I_{n,n} \end{bmatrix}. \tag{15}$$

Here $I_{i,j}$ is a pixel of the differential pupil image which is sampled by $n \times n$ pixels. For WFIRST LOWFS/C, the pupil sampling is $n = 16$ pixels. From Eq. (12), the vectorized differential image $\vec{\Delta I}$ and Zernike coefficient vector $\vec{Z}$ are related with a Zernike mode response matrix $\mathbf{K}$ as

$$\vec{\Delta I} = \mathbf{K} \cdot \vec{Z}. \tag{16}$$

The Zernike mode response matrix $\mathbf{K}$ can be generated with the modeled or experimental measured differential images with the known input amount of each Zernike mode applied to the system. For example, if we apply $\alpha = 1$ nm of each Zernike mode from Z2 to Z11 to the system and measure the differential images corresponding to each Zernike mode, we can build a response matrix $\mathbf{K}$ of size $n^2 \times 10$, where n^2 is the total number of pixels. We can then use the pseudoinverse of $\mathbf{K}$ to build a reconstruction matrix to detect WFE in the form of Zernike coefficients from the differential image $\vec{\Delta I}$:

$$\vec{Z} = \alpha^{-1}(\mathbf{K}^T\mathbf{K})^{-1}\mathbf{K}^T \cdot \vec{\Delta I}. \tag{17}$$

To keep the scale factor consistent, both reference and aberrated images need to be normalized before the images are differentiated. It is important to note that in this linear algorithm, the ZWFS sensing linearity range is limited to where the response matrix "training point" α is. WFE with amplitude significantly different from α will result in sensing error due to the nonlinearity. Therefore, $\mathbf{K}$ needs to be built with the training point α near where the WFE would be and α can be different for each Zernike mode. But as the analysis results presented in Sec. 4 have shown the ZWFS has g linearity range. For a Zernike mode response matrix $\mathbf{K}$ trained at $\alpha = 0.03$ nm, the ZWFS maintains linearity better than 1% over 10 nm. This is more than enough to cover a typical WFIRST WFE change.

In theory, $\mathbf{K}$ is assumed to be static during an observation, but in practice it is affected by dynamics and thermal effects. In Sec. 4, we summarize some of the numerical performance analysis of the LOWFS, and in particular the pupil registration errors due to the effects. Thermal effects can also change the linear dimensions of the FPM from thermal expansion of the materials. However, the Zernike mask itself is largely insensitive to changes in: (1) diameter of the phase mask (variations of $1.0\ \lambda/D - 1.6\ \lambda/D$ are acceptable) and (2) depth of the phase dimple ($+/-10\%$ errors are acceptable). Thermal changes are well within these loose tolerances.

3.2 *Wide-Field Infrared Survey Telescope Coronagraph Low-Order Wavefront Sensing and Control Subsystem*

WFIRST coronagraph LOWFS/C WFS is designed to use the rejected starlight from the coronagraph's focal plane occulting mask. The WFIRST OMC is convertible between two operating modes, HLC and SPC, and each configuration has its unique and complimentary science role and capability.[3] They require different FPMs selected by a filter wheel. Figure 5 shows the WFIRST OMC's conceptual optical layout. The coronagraph light passes through 2 DMs' starlight suppression masks unique to each mode of operation, and goes to the coronagraph's science camera or integral field spectrograph.[25] The rejected light, which contains almost all of the starlight, reflects off the FPM and is used for LOWFS/C wavefront sensing. One of the key features of the WFIRST LOWFS/C design is that the ZWFS's phase disk is designed and fabricated directly on the reflective side of the FPM. In other words, the FPM has dual functions: coronagraph starlight suppression mask in transmission and LOWFS/C ZWFS mask in reflection. This way, the starlight rejection and wavefront sensing occur at the same location. This not only ensures that the ZWFS measures WFE where the coronagraph needs it, but also avoids the noncommon path error on ZWFS since the light reflecting off the FPM contains both the reference WF and aberrated WF, and the subsequent LOWFS/C optics will be common to both.

The details of ZWFS mask design are different depending on the coronagraph mode. For HLC, the FPM acts as the occulter which has a reflective nickel spot of about 6 λ/D in diameter. On top of the nickel spot, facing toward the incoming beam,

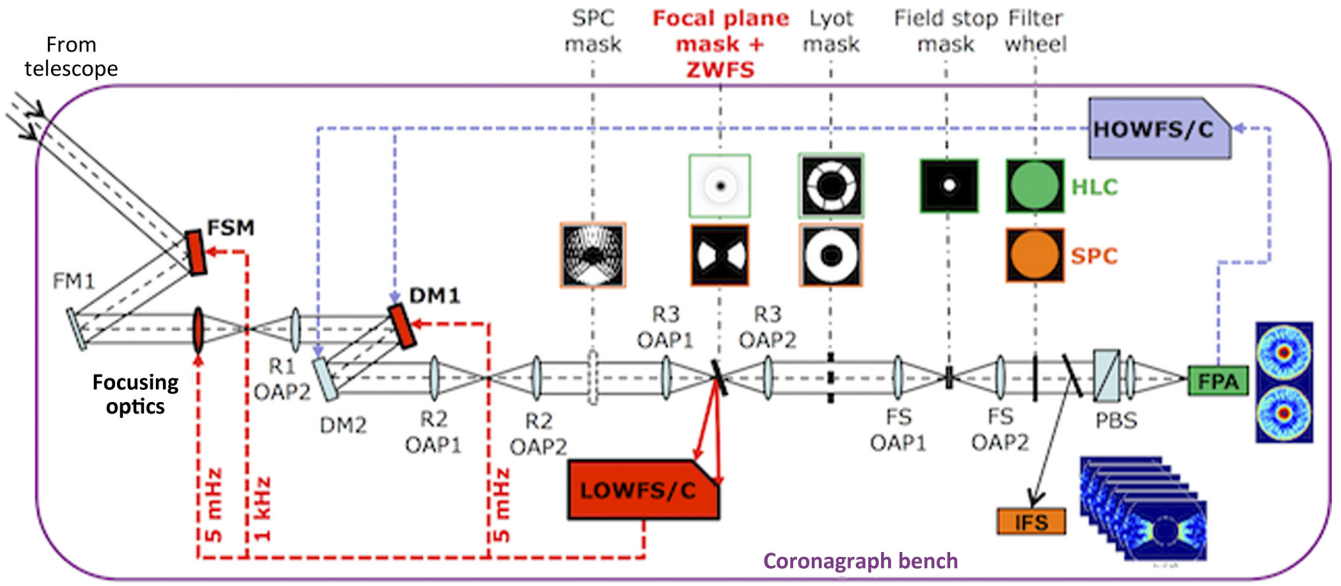

Fig. 5 Functional illustration of WFIRST CGI bench. Starlight from the telescope and relay optics enters CGI bench at left through the FSM. Two deformable mirrors (DM1, and DM2) correct the wavefront phase and amplitude for high-contrast imaging. Relay optics are off-axis parabolas (OAP). Focusing optics is a fold flat mirror on a linear actuator placed in the converging beam. The WFIRST CGI can operate in either HLC or SPC mode with HLC masks (top row with green borders) and SPC masks (bottom row in orange borders) being able to be switched in via filter wheels at pupil or image planes, indicated with dashed lines in the figure. A selectable mirror sends coronagraph light to either the imaging camera (FPA) behind a polarizing beam splitter (PBS) or the integral field spectrograph. The rejected starlight from the FPM, which has the LOWFS/C phase mask built-in, is captured by the LOWFS/C lenses and sent to LOWFS/C camera. The LOWFS/C subsystem, indicated by the red color components and lines, controls FSM, focusing optics, and DM1 with different updating speeds as labeled in their corresponding signal paths.

there is a dielectric layer with a complex radially symmetric profile.[20,6] At the center of this dielectric profile, a circular flat region of diameter $\sim 1.22\ \lambda/D$ is designed as a part of the profile with the thickness that creates a phase difference of $\pi/2$ for the light reflected within the $1.22\ \lambda/D$ region relative to the light reflected outside the region. (The diameter of $1.22\ \lambda/D$ was determined from a systematic analysis of performance over the radial size of the dielectric spot. It was determined to be optimal, but from $\sim 1.0\ \lambda/D$ to $\sim 1.6\ \lambda/D$, the performance degradation is negligible.) This unique dielectric profile design combines the needs of HLC and LOWFS/C's ZWFS. For SPC, the FPM is opaque inside the inner working angle and outside the outer working angle. The SPC's FPMs opaque regions are coated with nickel which reflects the rejected starlight to LOWFS/C. The center part of the nickel, where most of starlight is concentrated, is about $\sim 5\ \lambda/D$ in diameter. Depending on the SPC pupil mask (characterization or disc science) the SPC FPM is paired with, the light transmitting opening regions of SPC FPM can be either two wedge shaped areas, often referred as the "bowtie" mask as shown in Fig. 5, or a circular ring.[20] Unlike the HLC FPM, the ZWFS for SPC FPM is a simple circular dielectric phase disk with a diameter of $1.22\ \lambda/D$ deposited at the center of the SPC FPM on the reflective side. The dielectric layer thickness is designed to produce a phase difference of $\pi/2$ between the light reflected inside and that reflected outside the phase disk.

For LOWFS/C, the coronagraph's FPM acts as a low-pass spatial filter because of the limited size of the nickel spot, which is $\sim 6\ \lambda/D$ for HLC or $\sim 5\ \lambda/D$ for SPC. Therefore, the LOWFS/C ZWFS can only sense the low-order WFE and is insensitive to mid or high-spatial frequency WFE. Fortunately, as shown in Sec. 2, the dominant WFIRST WFE variation is low order in nature. Currently, LOWFS/C ZWFS senses the first 11 Zernike terms: tilts (Z2, 3), focus (Z4), astigmatisms (Z5, Z6), comas (Z7, Z8), trefoils (Z9, Z10), and spherical (Z11).

To pick up the light reflected from the occulter without blocking the incoming light, the coronagraph's FPM is slightly tilted. The FPM tilt angle is ~ 10 deg, small enough to avoid any significant projection distortion ($\sim 1.5\%$) for the transmissive coronagraph light, but large enough for LOWFS/C optics to gather the reflected light from the FPM. (Our studies have shown that the ZWFS is insensitive to the width of the phase dimple by factors much larger than $\sim 1.5\%$ from the ~ 10 deg angle of incidence effect.) The starlight reflected off the coronagraph's FPM is first collimated by a small lens and then relayed by another pair of lenses to form a pupil image on the LOWFS/C CCD camera. The pupil image formed is sampled by 16 pixels across the diameter. We choose to use lenses instead of mirrors as the LOWFS/C optics because they can form a compact, simple, and stable optical layout that meets the ZWFS imaging and stability requirements. The rejected starlight from coronagraph FPM is broadband. A fixed 20% spectral filter centered at 0.55 μm is placed in front of the CCD camera. Section 4 will discuss the spectral bandwidth selection for LOWFS/C in more detail.

The baseline LOWFS/C camera uses the E2V's CCD39 chip which has 80×80 pixels, four parallel readout ports, and a built-in TEC cooler. The CCD39 was chosen for its low noise ($4e^-$ read out noise), high-frame rate (1 kHz), and technology maturity—it has been flight-qualified by a previous project at JPL.[26] In our design, the LOWFS/C camera is running at a 1 kHz frame rate. The image data is read out and processed

Table 1 WFIRST LoS and WFE sensing and control summary.

Frequency/modes	Tip/tilt (Z2, Z3)	Focus (Z4)	Other modes (Z5 to Z11)
Wander (<2 Hz)	Sensing: ZWFS at 1 kHz	Sensing: ZWFS at 5 mHz	Sensing: ZWFS at 5 mHz
	Correcting: FSM at 1 kHz	Correcting: FM at 5 mHz	Correcting: DM1 at 5 mHz
Jitter (>2 Hz)		Recording ZWFS at 1 kHz	
		Coronagraph postprocessing	

by a real time computer. The WFE, in the form of 10 Zernike coefficients (Z2 to Z11), is computed at 1 kHz using the matrix multiplication expressed by Eq. (17).

The ZWFS sensed WFE is used to control corresponding wavefront correctors by the LOWFS/C, as shown in Fig. 5. The sensed tip-tilt (Z2, Z3) is used to drive the FSM control loop with an FSM command update rate of 1 kHz to suppress the LoS jitter and wander. Section 4.1 will discuss the FSM control in more detail. From Sec. 2, we can see that the WFEs other than tip-tilt are slow varying aberrations accumulating less than 30 pm/h. Thus, the ZWFS will time-average the sensed Z4 to Z11 over long period (minutes) to reduce the sensor noise without compromising the control bandwidth. The sensed focus term (Z4) is used to control the coronagraph's focusing mirror (FM) which is an actuated fold flat in a focused beam designed as a part of the CGI. Focus is one of the dominant modes of the WFIRST WFE budget. Correcting it with the dedicated FM will reduce the stroke burden on the DM. The remainder of the low-order WFE terms sensed by ZWFS are sent to a DM for correction. There are two DMs in the WFIRST coronagraph. The LOWFS/C uses DM #1, which is conjugated to the system pupil, as the WFE corrector to correct low-order WFE terms Z5 to Z11. A simple control architecture is defined to coordinate the LOWFS/C DM control and the coronagraph's dark hole generating HOWFS/C DM control when they concurrently operate. As a relative wavefront sensing and control system, the LOWFS/C is slaved to the HOWFS/C, which sets the LOWFS/C's reference wavefront.

In addition to LoS jitter the telescope vibration from the RWs will also cause WFE jitter with frequencies and amplitudes depending on the RW wheel speeds. The RW induced WFE jitters are dominated by a few low-order modes such as focus, astigmatisms, and comas. For the high-frequency (>2 Hz) wavefront jitters, the LOWFS/C does not have the bandwidth to suppress them. However, a portion of the WFE jitter effect on the coronagraph contrast can be removed by coronagraph data postprocessing. The ZWFS measurements will be recorded at 1 kHz rate together with the science data and will be transmitted to the ground as a part of engineering telemetry. They will be used for the coronagraph data-processing. From the recorded ZWFS data, we can also evaluate the uncompensated LoS and WFE jitters and use the information for data editing, discarding some science exposures in which the residual jitters are too large, as suggested by Guyon et al.[27] Table 1 summarizes the LOWFS/C sensing and control strategy for different WFEs in their corresponding spatial and temporal domains.

4 Numerical Performance Analysis

To analyze the performance of the ZWFS, an end-to-end diffraction model has been developed utilizing a semianalytical method.[28] The ZWFS uses the differential images between two pupil intensity measurements as per Eq. (12). Example images in Fig. 6 show the ZFWS modeling process. The interference of ZWFS turns the wavefront phase error at the entrance pupil into the intensity variation at ZWFS's camera. The intensity map that mimics the phase error map becomes obvious in the differentiated image when the DC components from the complex diffraction of the pupil geometry, DMs setting, and phase mask are removed. To model the ZWFS performance, a set of baseline modeling parameters that are consistent with the current coronagraph design have been used to represent the system. For photometry, a G type star is used for rejected starlight and the star magnitude varies from Mv = 0 to Mv = 8. The total effective system transmission is 0.24 which takes into account all of the WFIRST coronagraph optical element throughputs. The ZWFS spectral bandwidth is about 128 nm (more discussion on this later). The ZWFS pupil sampling is 16×16 pixels, which was chosen to optimize the sensor SNR and minimize WFE modes cross-talk. The detector model is based on the E2V CCD39 chip with $4e^-$ read out noise, $1e^-$ dark noise at 1 kHz frame rate, and about 80% to 87% quantum efficiency covering the 128 nm spectral band centered at 550 nm.

Our ZWFS model has three configurations: (1) the simple phase disk configuration, where the ZWFS FPM is just a $\pi/2$ phase disk of $\sim 1.22\ \lambda/D$ diameter while the PSF is generated from the WFIRST-AFTA pupil. This is used as a baseline for comparison with ZWFS for HLC and SPC; (2) the HLC configuration, where the FPM is the HLC occulter and both DMs have special patterns that are an integral part of the HLC design for the WFIRST coronagraph.[6] Because of the HLC DM patterns, the PSF formed on the occulter is no longer an ideal PSF from pupil diffraction as in configuration (1); (3) the SPC configuration, where an optimized shaped pupil mask creates a unique PSF with areas of high-starlight cancelation. The FPM is a bowtie shaped occulter with a $\pi/2$ phase disk of size $\sim 1.22\ \lambda/D$ in the center. The results reported in this paper are from the latest Gen 2 SPC pupil mask design.[20] We also studied another SPC configuration with the SPC discovery pupil mask and the circular FPM.[20] We do not report the results from the SPC discovery mask here since they are similar to the SPC bowtie FPM configuration.

4.1 *Zernike Wavefront Sensor Performance Analysis*

4.1.1 *Linearity*

Figure 7 shows the ZWFS linearity from the simple phase disk configuration (ZWFS configuration #1). The sensing linearity checks the linear dynamic range of the sensor response to the

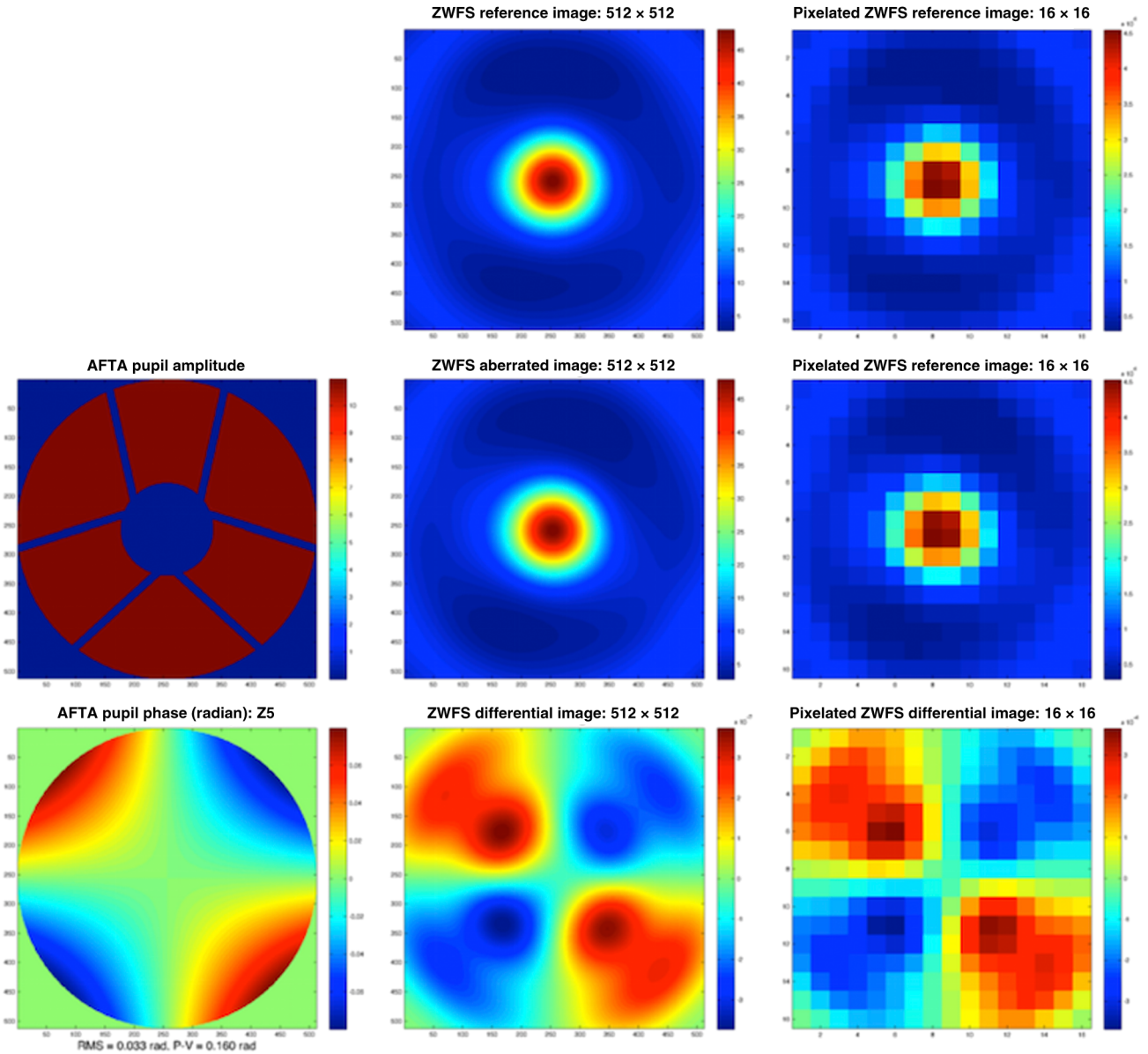

Fig. 6 Example images of ZWFS modeling process using the HLC configuration. The images on the left column are the amplitude and phase error at WFIRST-AFTA entrance pupil. Here, the phase error is the 45 deg astigmatism mode (Z5). The images in middle column are, from top to bottom, the high-resolution ZWFS reference (no phase error) image, the aberrated image, and the differential image. The images on the right are, from top to bottom, the corresponding pixelated (16 × 16 pixels) reference, aberrated, and differential images. The differential images mimic the phase error input and the pixelated differential image (lower right) is the signal $\Delta\vec{I}$ used for ZWFS sensing per Eq. (17).

injected aberration mode. The sensor linearity error is measured as the percentage of sensing error relative to the input. The plots in Fig. 7 show that the ZWFS sensing range can be as large as 10 nm RMS WFE with sensing linearity better than 1%. The relative sensing error plots for different Zernike modes show that focus and spherical aberrations tend to have higher-residual sensing errors, while tilt has the lowest-sensing error over the linear range.

4.1.2 *Cross-talk*

Figure 8 shows the sensing aberration mode cross-talk of the simple phase disk model which evaluates for a given Zernike aberration mode how much of the other Zernike modes are erroneously sensed by ZWFS. The plot in Fig. 8 shows that for most of the Zernike modes, the cross-talk is less than 1% when the input aberration is 1 nm RMS and the reconstruction matrix is built with the "training point" $\alpha = 0.03$ nm.

As discussed in Sec. 3.1, the ZWFS sensor has limited linearity range because the ZWFS algorithm linearizes the relationship between the WFE and the differential images intensity [Eq. (17)]. The sensor is mostly linear and cross-talk is small when the sensed WFE is near the response matrix "training point" α. For WFIRST LOWFS/C, we typically choose α to be ~0.1 nm typical for WFIRST WFE change. Although, Figs. 7 and 8 show the results from the simple phase disk configuration, the analysis using HLC and SPC configurations have shown similar behaviors.

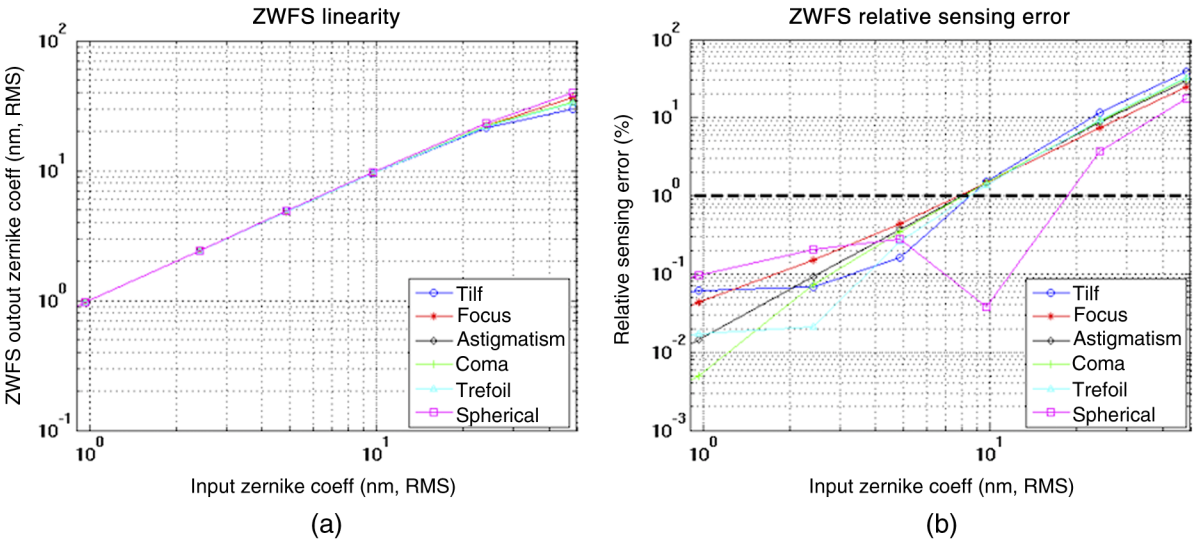

Fig. 7 ZWFS sensor linearity for a simple phase disk ZWFS. (a) The given and the sensed aberration modes with the input WFE expanding from 1 pm to 30 nm. (b) The percentage sensing error over the WFE range. For this analysis, the ZWFS **K** matrix is generated with $\alpha = 0.03$ nm, where the sensing error minimums occur on the curves on shown in the (b).

4.1.3 *Noise-equivalent pointing and wavefront errors*

One of the important ZWFS performance metrics is the noise equivalent sensing error. It measures how the sensor performs when the photon and detector noise are present. The ZWFS sensor noise performance analysis is done in the following steps:

1. The ZWFS model generates the ZWFS image with no aberrations.
2. Photon and detector noise are added to this image in 100 random realizations.
3. Choose any pair of aberration free but noise added images to generate the ZWFS differential image and reconstruct the corresponding Zernike coefficients. Since the image was generated when there was no WFE present, the sensed WFE is the noise equivalent sensing errors.
4. Take the average of the 100 random realizations of sensing error to obtain the mean RMS of tilts (Z2, Z3) and OPD (Z4 to Z11) sensing error to find the noise equivalent sensing error. The noise equivalent sensing error of tilt is converted to the noise equivalent LoS angles.

Figure 9 shows the noise equivalent LoS angle and noise equivalent sensing error for three ZWFS configurations.

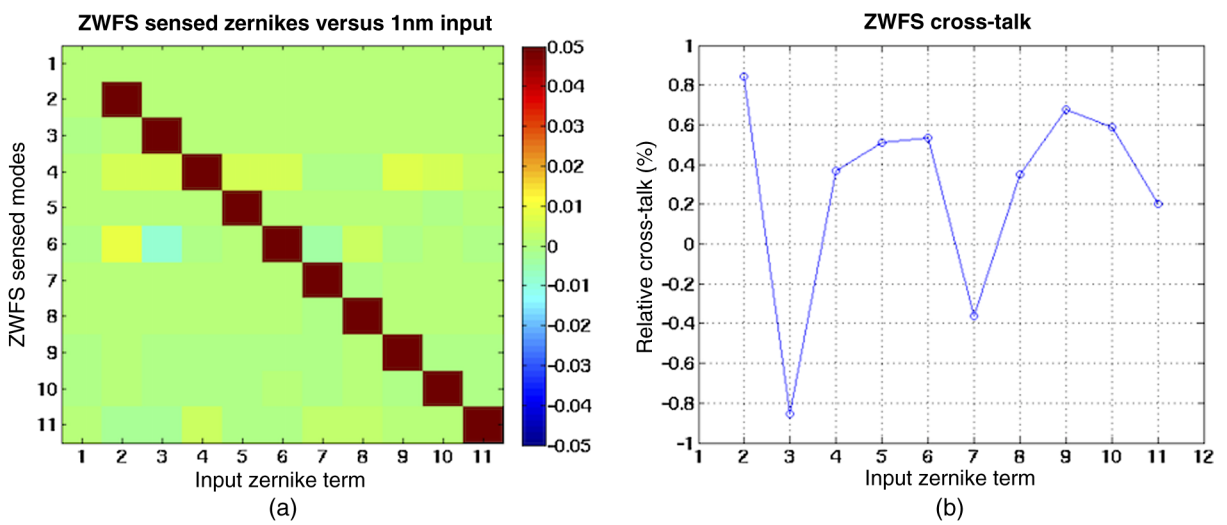

Fig. 8 ZWFS crosstalk for a simple phase disk ZWFS. (a) Cross-talk of Zernike mode sensed versus Zernike modes input. Each column represents the ZWFS response to a single Zernike input mode of 1 nm RMS. The color is stretched between −0.01 nm and +0.01 nm to accentuate the small cross-talk. For example, column 4 is for a 1 nm focus mode (Z4) input. The plot shows that besides Z4 the ZWFS also senses a small amount of spherical (Z11), which is from the sensor cross-talk of Z4 to Z11. (b) The ratio (percentage) of the worst cross-talk error relative to the input mode (1 nm).

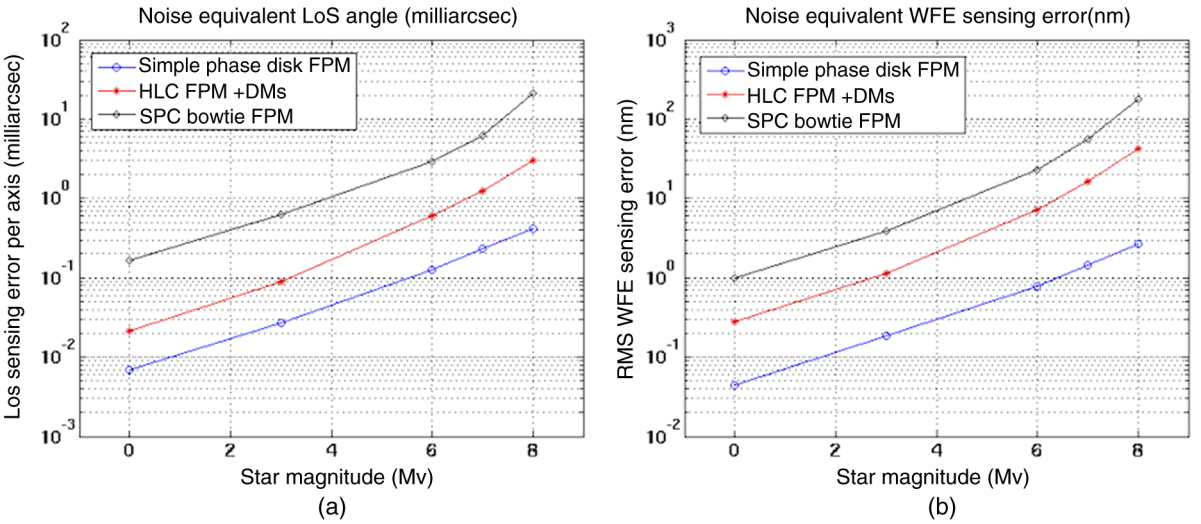

Fig. 9 ZWFS noise performance for a simple Zernike phase disk, HLC, and SPC configurations with the ZWFS camera running at 1 kHz frame rate. (a) The noise equivalent angle and (b) noise equivalent low-order WF sensing error.

Notice that the ZWFS noise sensing error is dominated by the photon noise with sensing errors and star magnitudes following a power law. Only for fainter stars of $Mv > 7$ do the noise curves begin to deviate from this power law, indicating that the detector noise becomes dominant. It is important to emphasize that this noise curve is evaluated at a camera readout rate of 1 kHz. For slowly varying low-order WFE, the sensor can gain a much greater performance through image averaging which is equivalent to increasing the stellar brightness. For example, if we average camera images so that the equivalent read out rate is one frame per minute, the exposure time increases by a factor of 60,000 and the equivalent stellar magnitude gain is $\Delta Mv \approx -12$. The 4 nm sensing error from an $Mv = 5$ star for HLC ZWFS will be reduced to 16 pm.

In addition to noise, there are many other factors that will also affect the ZWFS performance. We use the model to study the ZWFS performance against various parameters related to the ZWFS performance.

4.1.4 *Zernike wavefront sensor performance versus spectral bandwidth*

WFIRST ZWFS uses a dielectric phase disk at the center FPM to create a phase difference of $\pi/2$. This suggests that the sensor is inherently chromatic. For wavelengths other than the center wavelength, the phase delay is not exactly $\pi/2$. One might, therefore, expect a tradeoff between photon flux (from a broader spectral bandwidth) versus chromatic error from broadband light. However, this is not the case—the sensor continues to work well with very broadband light. Figure 10 shows the HLC ZWFS noise equivalent sensor error with different spectral bandwidths. The plots have shown that the ZWFS performance continues to improve with photons.

4.1.5 *Zernike wavefront sensor image registration*

During the ZWFS measurement, two intensity images, reference and measured, will be taken at different times. If the LOWFS/C

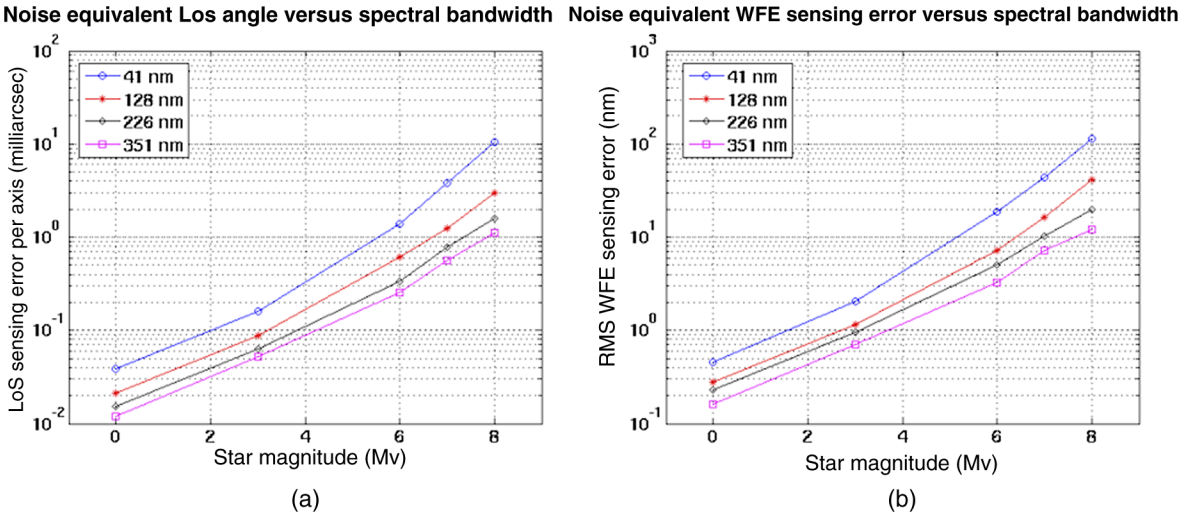

Fig. 10 ZWFS (HLC configuration) performance versus sensor's spectral bandwidth. (a) The effect on noise equivalent angle and (b) low-order WFE sensing error.

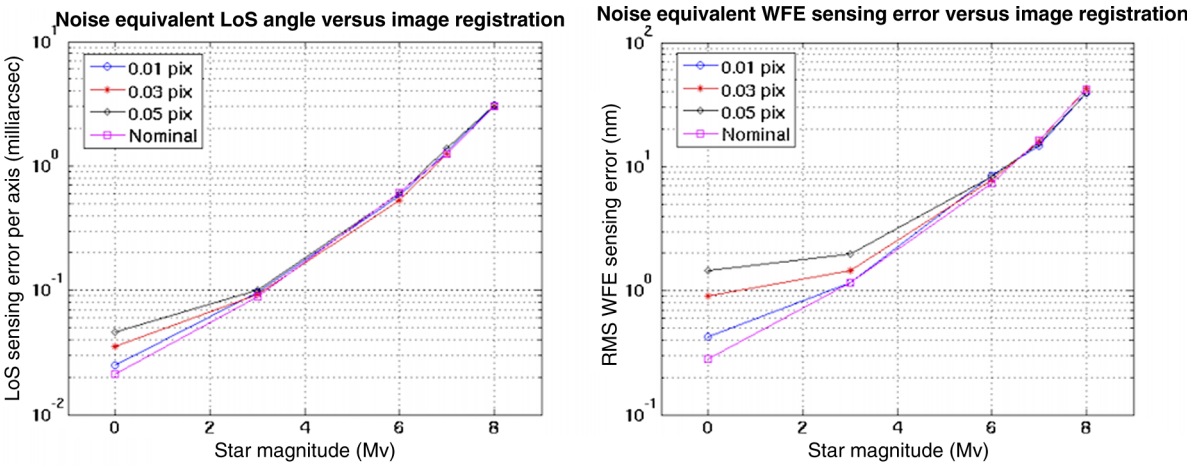

Fig. 11 ZWFS (HLC configuration) performance versus image misregistration. (a) The effect on noise equivalent angle and (b) low-order WFE sensing error.

imaging optics are not stable, causing the two images to shift relative to each other, the misregistration between the reference and measurement images will cause ZWFS sensing error. We have studied the ZWFS sensitivity to the image misregistration by creating subpixel shift between the two images in the sensor noise performance modeling. Figure 11 shows the result. Unlike the sensor error from the photon noise (Fig. 9), the sensor error from the misregistration cannot be reduced by simply coadding the frames or a longer exposure. From the plots, we can see that the ZWFS is quite sensitive to the image misregistration. For the ZWFS to perform at 10 s of pm level, the ZWFS image registration needs to be stable to ~0.01 pixel. Fortunately, the ZWFS uses pupil image so the image position is not affected by WFE or LoS tilt. Furthermore, the ZWFS has a very coarse sampling, 16 pixels across the entire telescope pupil, so this level of registration stability is not prohibitively strict. Nevertheless, this still requires the LOWFS/C imaging lenses to be stable within 0.25 μm in translation and FPM tilt within 10 μrad during the LOWFS/C operation.

4.1.6 *Zernike wavefront sensor performance versus the detector read-out noise*

The impact of ZWFS camera read out noise is shown in Fig. 12. The ZWFS HLC configuration performance is evaluated with cameras that have: $0.3e^-$, $4e^-$, or $7.5e^-$ read out noise. As expected, as the camera read out noise increases, the ZWFS performance degrades.

4.2 *Line-of-Sight Jitter Sensing and Control Design and Performance Analysis*

The LoS control loop is used to stabilize the wavefront tip and tilt (Z2 and Z3) using the measurements provided by the LOWFS/C sensor. This is done using a FSM with piezoelectric actuators made of lead zirconate titantate (PZT). The FSM, developed for the SIM project,[19,29] has an angular stroke of $\pm$82.5 arcsec, which is equivalent to $\pm$3.2 arcsec LoS on the sky for the WFIRST coronagraph, and is fitted with strain gauge sensors that can be used to remove the hysteresis of

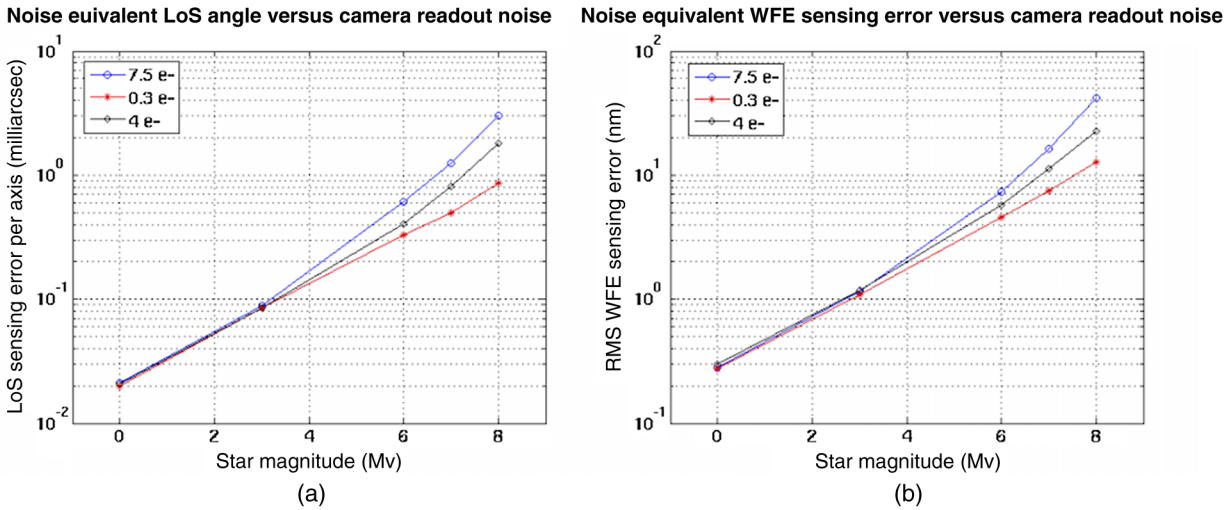

Fig. 12 ZWFS (HLC configuration) performance versus detector read out noise. (a) The effect on noise equivalent angle and (b) low-order WFE sensing error.

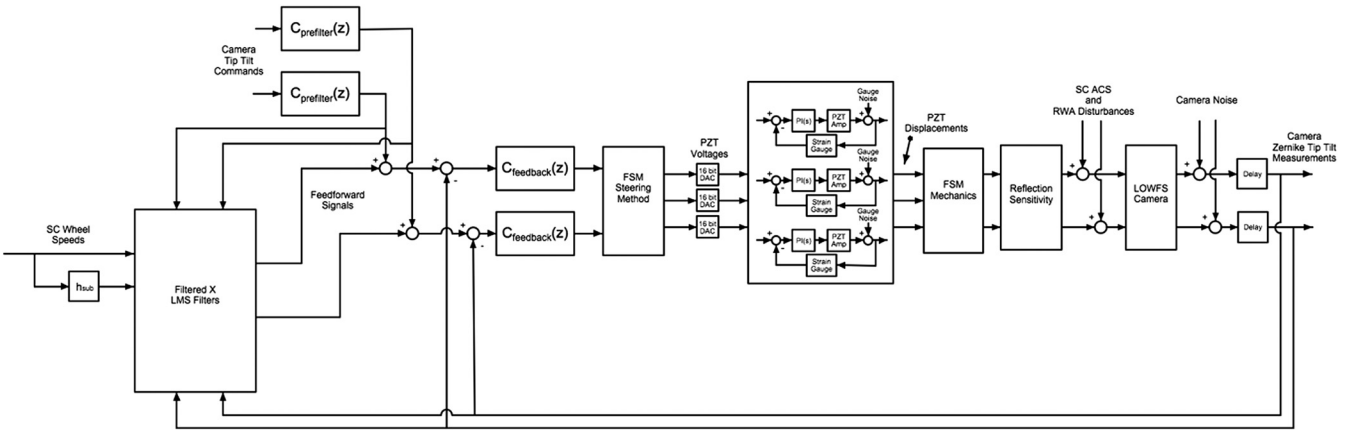

Fig. 13 LOS control concept. Current sampling rate from the LOWFS/C camera is 1000 Hz with 1.5 integration cycles of delay.

the PZT actuators. The strain gauge loop is an analog loop with a bandwidth of 200 Hz that can be adjusted. The FSM has a six degree of freedom momentum compensated design with a tip and tilt first resonance mode of ~900 Hz.

The frequencies and magnitudes of the expected LoS error inputs and coronagraph sensitivities to them were discussed in Sec. 2. Figure 13 shows the control scheme of LoS control for the WFIRST coronagraph using the LOWFS/C camera and FSM. The first stage of suppression uses a feedback control loop. The bandwidth of this loop is limited by the sample rate, delays, and noise of the camera measurements. The current baseline is to use a sample rate of 1000 Hz for the LOWFS/C camera. Camera noise associated with the fainter star could necessitate further reductions in the bandwidth of this loop. The feedback loop servo loop is tailored to suppress the low-frequency LoS wander from ACS (<2 Hz) and to reduce the ZWFS sensor noise. All LoS jitters from RW are to be suppressed by a feedforward loop. Based on the structural analysis of the LOS jitter due to wheel harmonics, the amplitude of the RWA disturbance exceeds the 0.4 mas requirement over many of the expected wheel speeds (Fig. 1). The feedforward loop in Fig. 13 is currently under consideration to address this issue. This path extends the bandwidth over which disturbances can be attenuated. This is achieved by estimating the disturbance using measurements of the signal before and after the disturbance. In addition, knowledge of the wheel speed from ACS can be used to give the frequency of the disturbance, leaving only the gain and phase of each disturbance tone to be estimated. We are currently investigating the best way to implement the feedforward control. Options include using a Kalman filter to estimate parameters of the disturbance signal or using a disturbance observer to directly reconstruct the disturbance signal. It should be mentioned that not all of the disturbance tones coming from the RWA assembly need to be estimated. For most wheel speeds, only the first two wheel tones, the fundamental tone and the first subharmonic, need to be removed. Moreover, these tones only need to be rejected with 10% accuracy to meet requirements. However, the feedforward approach does rely, to some extent, on a linear FSM actuator since the actuator response must be inverted once the disturbance signal is known. Linearization of the FSM actuators is achieved by using the strain gauge feedback. Strain gauges are mounted on the PZT stacks of the FSM. These sensors are used with an analog compensator to linearize the PZT hysteresis to an accuracy of less than 1%. Special PZT control electronics that use a modulation/demodulation technique are used to implement this analog loop to ensure that the jitter caused by strain gauge noise is minimized.

Figure 14 and Table 2 summarize the modeled FSM loop performance against the WFIRST RW induced jitter shown in Fig. 1. We remind the reader that these performance models assume: a sample rate of 1 kHz, a training point of the ZWFS of 30 pm, a closed-loop tailored to suppress low-frequency LoS errors, and feedforward for addressing high-frequency errors. In this model, we use the ZWFS sensor noise model for the HLC configuration shown in Fig. 9, as well as the measured FSM noise. The plot shows that the residual jitter depends on the sensor noise which is a combination of photon noise from the star (magnitude dependent) and the detector read noise.

Table 2 shows the fraction of time over which the residual jitter meets three coronagraph performance evaluation criteria, assuming that wheel speed distribution is uniform from 10 to 40 rev/s. The modeled results are preliminary and the controller's parameters still need to be further optimized.

Figure 14 and data in Table 2 show that the residual jitter can meet the most stringent 0.4 mas requirement most of time, except when the star is fainter than Mv = 7. For these targets, we can rely on the data editing option which discards the science exposures taken when the jitter was high according to the LOWFS/C telemetry. This topic is discussed in detail in a companion article in this issue[30] in the context of PIAACMC science performance, where this data editing scheme provides the largest benefit of all coronagraph architectures.

4.3 *Low-Order Wavefront Error Control with the Deformable Mirror*

We have developed a LOWFS/C model based on the design of the HLC and the characteristics of ZWFS to simulate the closed loop LOWFS/C WFE control using the DM #1.[31] The model takes the low-order portion of wavefront variation from the structure, thermal, and optics model in the form of Zernike coefficients as input. It also tracks the residual low-order WFE arisen from the FSM LoS correction and focus correction due to the beam walks, as well as the imperfection of DM control in the previous iteration of WFE correction. All these WFE terms are being fed into a ZWFS sensor model for current iteration WFE estimation and control. The postcorrected residual WFE, which includes DM fitting errors from the DM gain

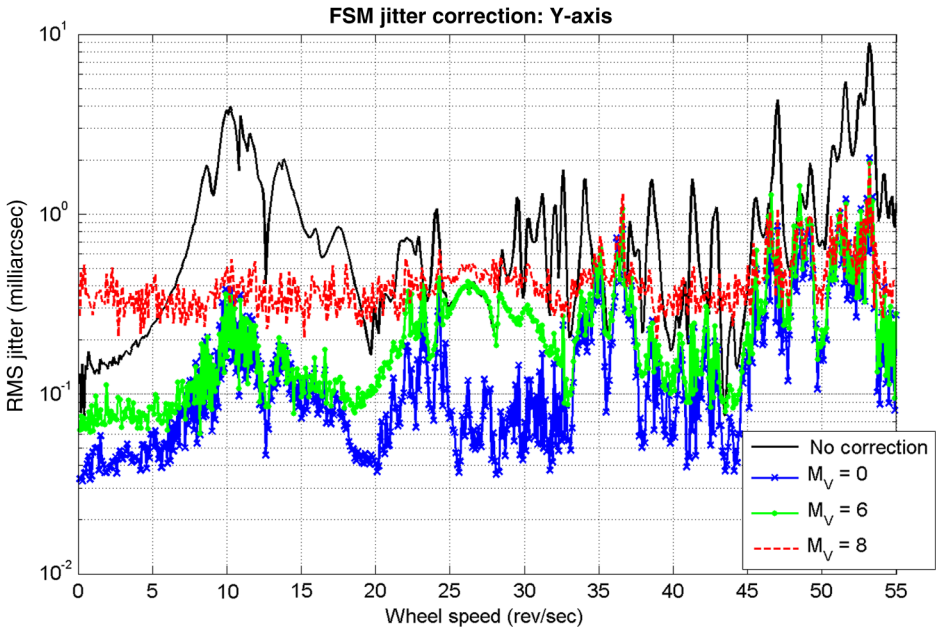

Fig. 14 WFIRST jitter input and the residual LoS jitter with the LOWFS/C FSM loop plotted against the RW wheel speed. The plot shows the Y axis LoS jitter.

Table 2 Percentage of time the residual jitters meet the three coronagraph performance evaluation criteria.

Star magnitude (Mv)/jitter (mas)	X jitter residual over 10 to 40 rev/s			Y jitter residual over 10 to 40 rev/s		
	≤0.4	≤0.8	≤1.6	≤0.4	≤0.8	≤1.6
0	95%	98%	100%	97%	100%	100%
3	95%	98%	100%	97%	100%	100%
6	83%	98%	100%	93%	100%	100%
7	83%	98%	100%	91%	99%	100%
8	59%	97%	100%	52%	99%	100%

calibration errors, is fed into the HLC coronagraph model to evaluate the coronagraph performance in terms of coronagraph contrast and contrast changes.

The DM actuator height versus control voltage curve of each actuator is nonlinear and these curves are slightly different for each actuator. Each DM actuator's gain will be calibrated around its bias voltage, but some calibration error is inevitable. We carried out an investigation to determine how tight the requirements on DM actuator gain knowledge have to be in order to use the DM for correcting low-order WFE terms above focus without unacceptably degrading the coronagraph contrast. To understand the impact of such actuator gain-errors on the LOWFS/C, we introduced two types of actuator gain-error factors: the static gain-error factors of $\vec{\delta}_s$ and time-varying or dynamic gain-error factors of $\vec{\delta}_{d_i}$, that is

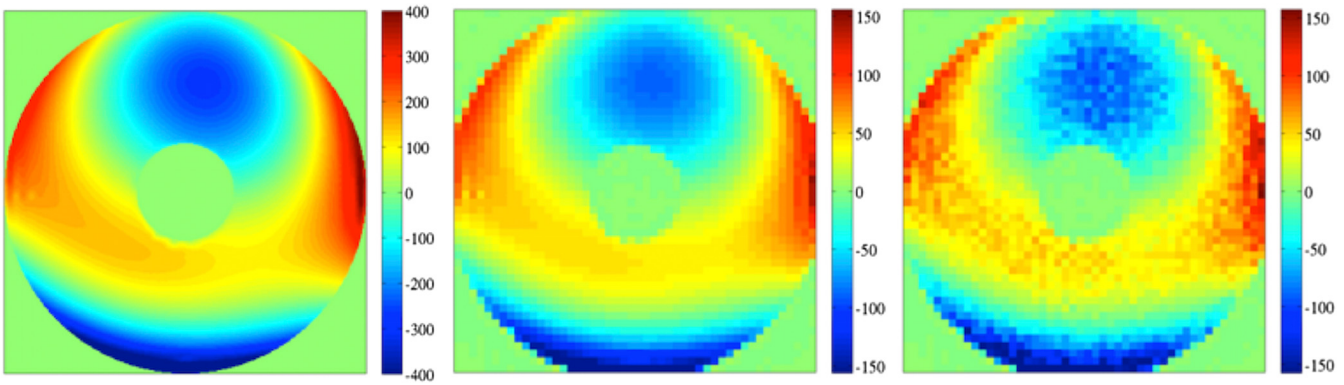

Fig. 15 Example of DM actuator height map with and without the DM gain calibration error. In this example, the DM is trying to compensate the WFE error from the WFIRST-AFTA telescope variation, which is the OPD map on the left. The sign of OPD is flipped in this plot for easy comparison with the DM height maps. On the DM actuator height maps (middle and right plots) each pixel represents the height of one actuator in a 48×48 actuator DM. The DM actuator height map in the middle is from DM control without DM gain calibration error while the actuator height map on the right is from the DM with actuator gain calibration error of $\vec{\delta}_s =$ 20% and $\vec{\delta}_{d_i} =$ 10%.

$$\vec{u}_{g_i} = \vec{u}_{\mathrm{DM}_i}(1+\vec{\delta}_s)(1+\vec{\delta}_{d_i}), \tag{18}$$

where $\vec{u}_{\mathrm{DM}_i}$ is the desired LOWFS/C DM command for the current iteration DM control (denoted by subscript i) and $\vec{u}_{g_i}$ is the actual DM poke the actuator realized, which includes the DM actuator gain-error factors. In the model, we assume the DM actuator static gain calibration error $\vec{\delta}_s$ is spatially randomly distributed among the DM actuators, while the time varying gain error $\vec{\delta}_{d_i}$ is temporally incoherent, both error terms are proportional to the DM stroke and are added on top of the desired DM stoke.

Figure 15 illustrates the effect of the DM gain calibration error. It shows that the DM gain calibration error will cause post LOWFS/C correction residual WFE to fall into mid to high-order spatial frequency because the DM actuator gain calibration error is, in general, random among the actuators. The LOWFS/C sensor, however, will not be able to sense these mid to high-spatial frequency DM residual errors due to its limitation in spatial resolution. Therefore, using a DM to correct the

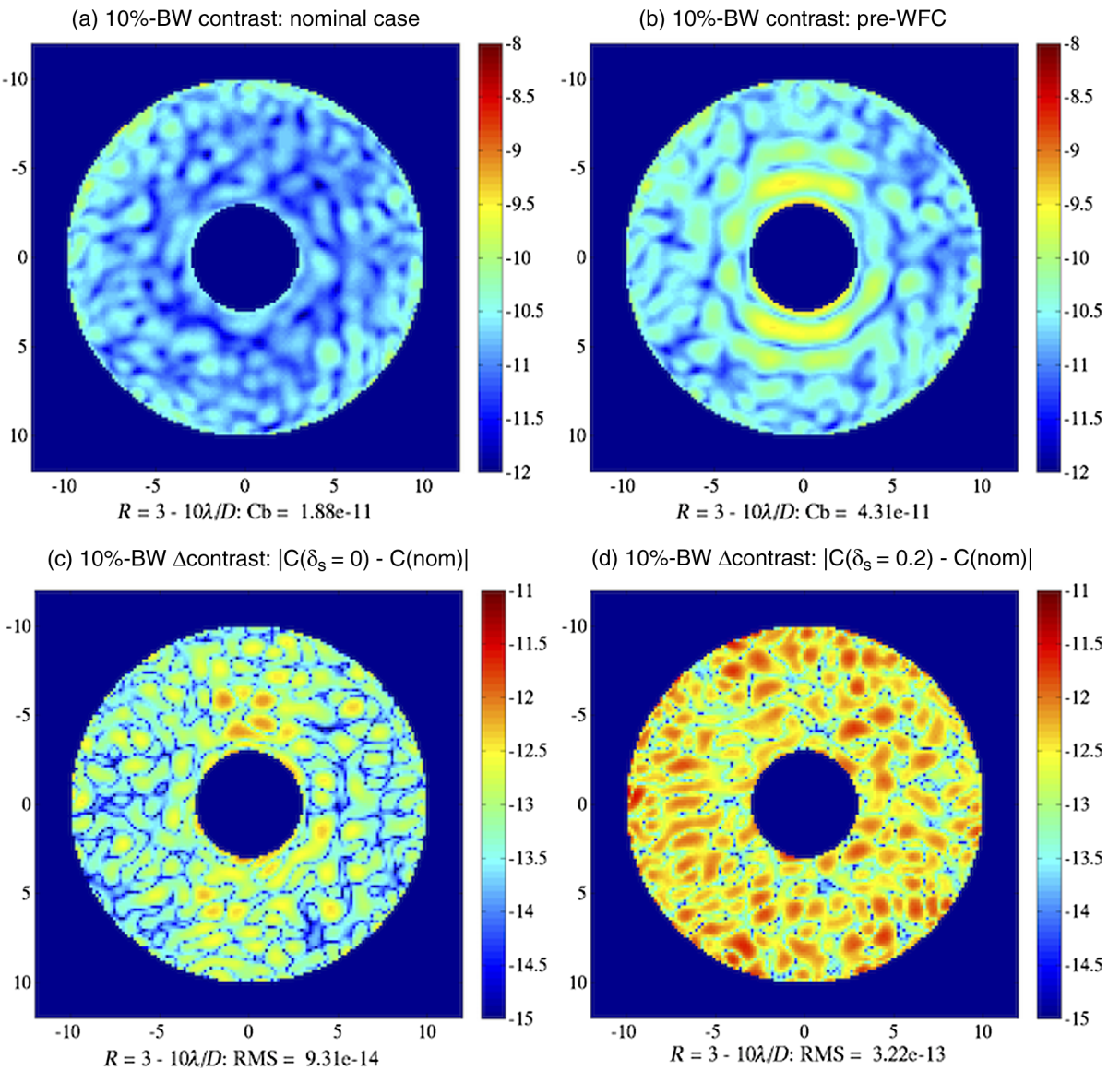

Fig. 16 (a) Nominal 10% broadband contrast map achieved after a HOWS/C process called electric-field conjugation. (b) Introducing 47.2 pm coma (Z7) wavefront error to the WFIRST-AFTA pupil changes the coronagraph contrast map from nominal (a) to this one. After single-iteration LOWFS/C correction using DM1 without any actuator gain calibration error ($\vec{\delta}_s = 0$, $\vec{\delta}_{d_i} = 0$) results in a new contrast map. (c) The absolute difference between the post LOWFS/C DM control contrast map and the nominal contrast map (a). "RMS" in the x-label is the root-mean-square value of the corresponding contrast map difference, averaged over 3 – 10 λ/D. (d) Contrast map difference after LOWFS/C control using DM1 with 20% static ($\vec{\delta}_s = 20\%$) and 10% dynamic ($\vec{\delta}_{d_i} = 10\%$) actuator gain errors. Note that the (a) and (b) show the contrast while the (c) and (d) show the absolute contrast difference. All maps are plotted in log-scale. In this simulation we only looked at the DM control of a static WFE (Z7). The simulation does not include any LOWFS/C sensor error or WFE dynamics.

low-order WFE commanded by the LOWFS/C may adversely affect the coronagraph's performance because these mid to high-spatial frequency WFE will cause extra speckles in the coronagraph dark hole field and degrade the coronagraph contrast. The contrast examples in Fig. 16 clearly illustrate this degradation. The plots in Fig. 16 shows the contract and its changes from an ideal coronagraph without any other system imperfection except the effect of diffraction. The plots are to illustrate the relative changes of contrast against DM gain calibration error, where the absolute contrast floor is unimportant in this case. From Fig. 16, we can see that the contrast difference from the LOWFS/C control using DM with actuator gain errors [Fig. 16(d)] is much worse than that without DM actuator gain error [Fig. 16(c)].

We use the LOWFS/C model to simulate the LOWFS/C closed loop sensing and control using DM1 for the thermally induced WFIRST WFE variation shown in Fig. 2. While the DM is capable of correcting low-order (Z5 to Z11) WFE, the DM gain calibration error will introduce the mid to high-spatial frequency error which directly affects the coronagraph contrast as the plots in Fig. 17 have indicated. Figure 17 plots the RMS contrast difference with different DM actuator gain errors when the DM is used to correct the same thermal variation shown in Fig. 2. In this simulation, the LOWFS/C sensing error is reasonably small, using an Mv = 5 star and integration of 1000 s, so we can compare the DM gain error impact. From Fig. 17, we can see that for a typical WFIRST WFE variation, if we wish to maintain the contrast stability to $\sim 2 \times 10^{-10}$ level, we need to calibrate the DM actuator gain to better than 10% ($\vec{\delta}_s = 0.1$). Furthermore, because in our model we have defined the DM gain error as the proportional term to the DM stroke, as expressed in Eq. (18), if the WFE variation is larger, the DM calibration requirement will be even tighter. Otherwise, we would have to rely on the "data editing" to discard the coronagraph science data when the variation is too large.

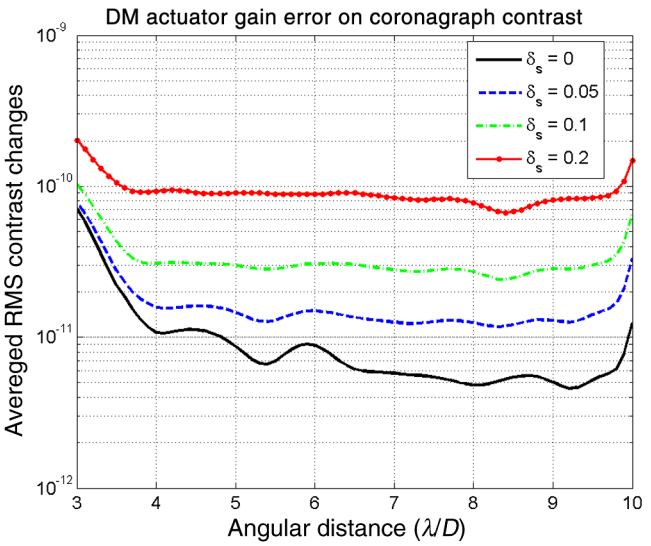

Fig. 17 HLC radial averaged contrast changes, which is the RMS of contrast difference between the post correction and nominal contrast map, are plotted against the coronagraph field of view. Contrast is 10% broadband. Each curve represents the mean contrast changes averaged over the time period of 56 hours in which the LOWFS/C DM correction loop is closed to cancel the thermally induced WFE variation shown in Fig 2. The curve with different colors are from the LOWFS/C control using the DM with different actuator gain calibration errors as the legend indicated. In the simulation the static gain calibration error varies from $\vec{\delta}_s = 0$ to $\vec{\delta}_s = 0.2$ while the dynamic gain error $\vec{\delta}_{d_i}$ is always § of static error.

5 Preliminary Vacuum Low-Order Wavefront Sensing and Control: Testbed Overview and Preliminary Results

To demonstrate and evaluate the performance of LOWFS/C with HLC and SPC coronagraph modes under the representative WFIRST environment, we have designed an optical telescope assembly (OTA) simulator to inject the expected WFIRST wavefront variation and LoS jitter into the OMC coronagraph testbed. This system and its characterization and performance will comprise a separate paper. Here, we provide a brief overview of the architecture and the preliminary tit/tilt results.

The OTA simulator acts as the coronagraph testbed star source, providing point source light with various brightness and spectral bandwidth. It also creates the pupil shape that mimics the obscured 2.4 m WFIRST-AFTA telescope. Before the OTA simulator is delivered to the OMC coronagraph testbed, it will be first tested on the LOWFS/C testbed. Figure 18 and its caption describe the optical layout and functions of the OTA Simulator and LOWFS/C testbed.

The OTA simulator relies upon the precision linear movement of the powered optics (telescope, SM, OAP2) to generate small (sub nm) low-order WFE. Pure low-order aberration modes such as focus, coma, astigmatism, and spherical can be generated by properly moving a powered optical mirror. For example, by tilting and translating an offaxis parabola mirror (OAP2) one can generate pure astigmatism. For a small perturbation, the amplitude of the aberration mode is proportional to the movement of the optics. To accurately move the powered optics, we use PZT actuators with strain gauges, which can provide microns of motion with sub-nm precision and linearity better than 0.2%. Optical design software is used to create the aberration sensitivity to these powered optics from their six degree of freedom perturbations and derive the PZT commands needed to generate the desired aberration mode.

The LOWFS/C testbed optics including OTA simulator subbench sit on a 3′×4′ optical bench. The LOWFS/C tests will be conducted in a small vacuum chamber with air legs to remove the air turbulence and ambient vibration, and an MLI thermal blanket to provide good thermal stability. On the LOWFS/C testbed, we will demonstrate the LOWFS/C sensor performance and close the FSM loop to suppress the LoS jitter injected by JM, as well as the focusing control loop using the FM. The LOWFS/C control of Z5 to Z11 errors with DM will be conducted later on the OMC testbed because we need a coronagraph to evaluate the DM gain error impact on contrast. We have finished the OTA simulator and LOWFS/C testbed building and alignment.

Figure 19 illustrates the preliminary tip/tilt performance of the LOWFS/C system in this testbed. These tip/tilt measurements are made in the testbed described above, and cover three different conditions: (1) open loop lab noise, (2) injected ACS variation, and (3) closed-loop operation using the ZWFS to drive the FSM to correct for pointing errors. When the loops are closed, the tilt errors are ~0.22 mas for X-tilt and ~0.27 mas for Y-tilt [excluding high-frequency (>200 Hz) lab noise]. The system is operational and the preliminary performance is

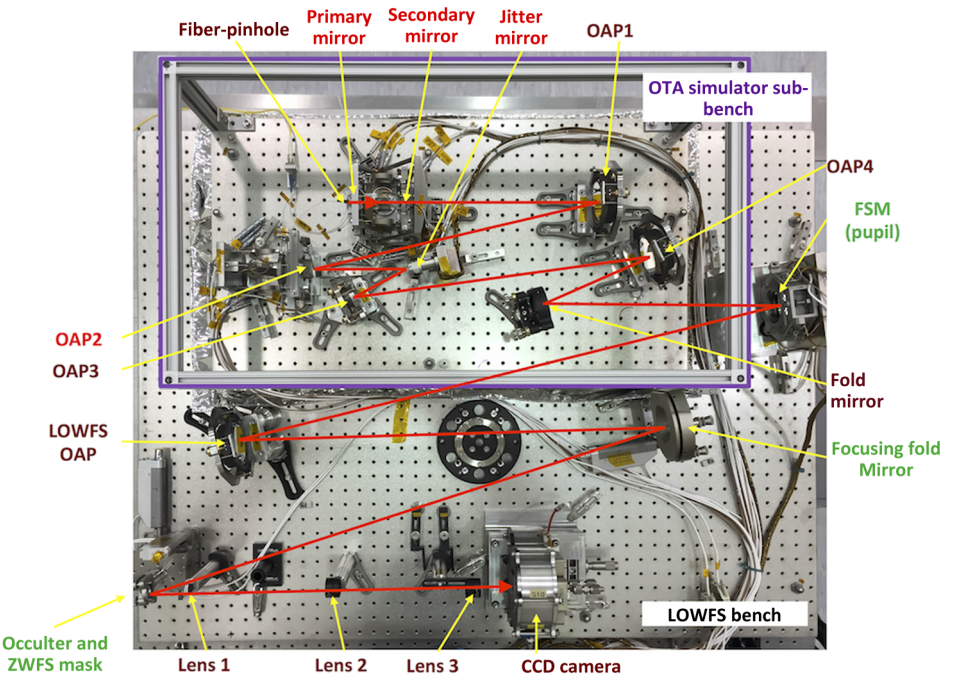

Fig. 18 The optical configuration of the OTA Simulator and the LOWFS/C testbed is shown above. The OTA simulator uses a fiber-illuminated pinhole as the star. The light from the pinhole is collimated by a miniature telescope with the scaled down WFIRST-AFTA telescope primary mirror and secondary mirror. A pupil mask behind the secondary mirror support creates the WFIRST-AFTA pupil shape, which has the SM obscuration and the shadows of the SM supporting struts. A pair of OAPs (OAP 1 and 2) relays this pupil to the jitter mirror (JM). The JM is a small, 1-in. flat mirror on a PZT tilt stage with integral strain gauge sensors. It is used to inject the high frequency LoS jitter into the system. After the JM, another pair of OAPs (OAP 3 and 4) create a collimated beam and form a pupil just outside the OTA Simulator sub-bench for interface with the testbed interface optics, which on the LOWFS/C testbed is the FSM. In OTA Simulator the miniature AFTA telescope, SM, and OAP2 are all actuated in 6 degree of freedoms by PZT actuators with strain gauges to create the needed low order WFE modes, simulating the WFIRST-AFTA WFE variation. The LOWFS/C testbed starts with the FSM. The following LOWFS OAP creates F/30 focused beam on the ZWFS mask. The beam is folded by a flat mirror on a linear stage, which serves as the focus correcting mirror. The ZWFS light reflects from FPM and is collected and collimated by lens 1 and reimaged to LOWFS/C CCD camera by lens 2 and 3. They form a pupil of 16×16 pixels on the LOWFS/C CCD camera.

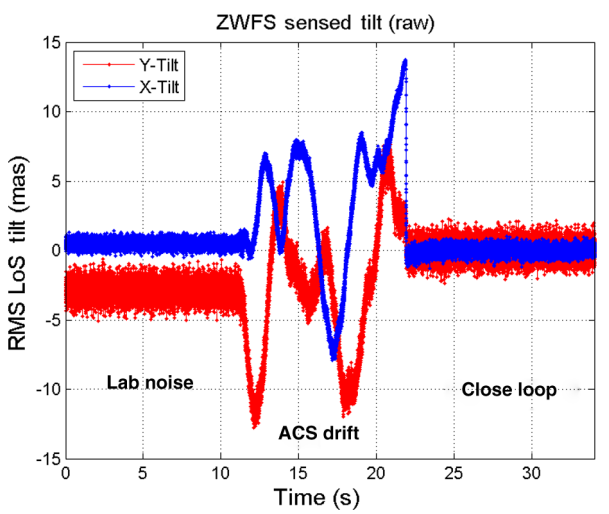

Fig. 19 The preliminary tip/tilt sensing and control performance of the LOWFS/C is shown for three different states: (1) open-loop, which includes noise sources both inside and outside the control bandwidth of the system, (2) with ACS variation injected into the system, and (3) in closed-loop with the FSM removing both ACS variation and environmental disturbances within the control bandwidth of the system. This preliminary result does not implement feed forward. Please note that that postresidual correction in *Y*-tilt is the high-frequency lab noise.

traceable to the requirements for the final mission. A subsequent paper will quantify and characterize the performance of the LOWFS/C in greater detail.

6 Conclusion

WFIRST coronagraph requires a LOWFS/C subsystem to maintain the coronagraph's contrast stability. The Zernike phase contrast WFS is selected to sense the low-order wavefront variation and LoS jitter using the starlight rejected by the coronagraph's FPM. Working in the differential image mode, the ZWFS can provide the sensitivity needed to sense and correct the expected WFIRST LoS jitter and wavefront variation. Simulations of LOWFS/C closed loop jitter suppression and low-order WFE correction have been done for the realistic disturbances generated by the current observatory models and on-orbit operating scenarios. The fidelity of these observatory models will increase over time, but the initial results are encouraging. A testbed is being built to simulate WFIRST-AFTA telescope LoS jitter and wavefront variation and to perform stand-alone testing of the LOWFS/C subsystem before integrating it with the coronagraph. The early lab results using an HLC FPM have shown that the ZWFS sensor is capable of detecting submilliarcsecond tilt, as needed for WFIRST coronagraph to meet its science

requirements. The successful lab test of ZWFS has brought the sensor technology to TRL 4.

Acknowledgments

The work published in this paper is supported by NASA's WFIRST mission study office. The authors also are grateful for the contributions of many scientists and engineers on the WFIRST coronagraph team. We are especially grateful for the valuable advice from Prof. Olivier Guyon of the University of Arizona. This research was carried out at the Jet Propulsion Laboratory, California Institute of Technology, under a contract with the National Aeronautics and Space Administration.

References

1. Committee for a Decadal Survey of Astronomy and Astrophysics, *New Worlds, New Horizons in Astronomy and Astrophysics*, The National Academies Press, Washington, DC (2010).
2. P. R. Lawson et al., "Survey of experimental results in high-contrast imaging for future exoplanet missions," *Proc. SPIE* **8864**, 88641F (2013).
3. F. Zhao et al., "WFIRST-AFTA Coronagraph instrument Overview," *Proc. SPIE* **9143**, 91430O (2014).
4. L. Harding et al., "Technology advancement of the CCD201-20 EMCCD for the WFIRST-AFTA coronagraph instrument: sensor characterization and radiation damage," *J. Astron. Telesc. Instrum. Syst.* **2**(1), 011007 (2015).
5. J. Krist, B. Nemati, and B. Mennesson, "Numerical modelling of the proposed WFIRST-AFTA coronagraphs and their predicted performances," *J. Astron. Telesc. Instrum. Syst.* **2**(1), 011003 (2015).
6. J. Trauger et al., "Hybrid Lyot coronagraph for WFIRST-AFTA: coronagraph design and performance metrics," *J. Astron. Telesc. Instrum. Syst.* **2**(1), 011013 (2015).
7. D. Savransky and D. Garrett, "WFIRST-AFTA coronagraph science yield modeling with EXOSIMS," *J. Astron. Telesc. Instrum. Syst.* **2**(1), 011006 (2015).
8. T. Groff et al., "Methods and limitations of focal plane sensing, estimation, and control in high-contrast imaging," *J. Astron. Telesc. Instrum. Syst.* **2**(1), 011009 (2015).
9. O. Guyon, "Limits of adaptive optics for high-contrast imaging," *Astrophys. J.* **629**, 592 (2005).
10. A. Give'on et al., "Broadband wavefront correction algorithm for high-contrast imaging system," *Proc. SPIE* **6691**, 66910A (2007).
11. J. Hardy, *Adaptive Optics for Astronomical Telescopes*, Oxford University Press, New York (1998).
12. R. Ragazzoni, "Pupil plane wavefront sensing with an oscillating prism," *J. Mod. Opt.* **43**, 289 (1996).
13. J. K. Wallace et al., "The gemini planet imager calibration wavefront sensor instrument," *Proc. SPIE* **7736**, 77365D (2010).
14. J. R. P. Angel, "Ground-based imaging of extrasolar planets using adaptive optics," *Nature* **368**, 203 (1994).
15. E. E. Bloemhof and J. K. Wallace, "Phase contrast techniques for wavefront sensing and calibration in adaptive optics," *Proc. SPIE* **5169**, 309–320 (2003).
16. O. Guyon, T. Matsuo, and R. Angel, "Coronagraphic low-order wavefront sensor: principle and application to a phase-induced amplitude coronagraph," *Astrophys. J.* **693**, 75 (2009).
17. G. Singh et al., "Lyot-based low order wavefront sensor for phase-mask corongraphs: principle, simulations and laboratory experiments," *PASP* **126**(940), 586–594 (2014).
18. J. K. Wallace et al., "Phase-shifting zernike interferometer wavefront sensor," *Proc. SPIE* **8126**, 81260F (2011).
19. R. Goullioud et al., "The SIM lite astrometric observatory: engineering risk reduction activity," *Proc. SPIE* **7734**, 77341M (2010).
20. K. Balasubramanian et al., "WFIRST-AFTA coronagraph shaped pupil masks: design, fabrication and characterization," *J. Astron. Telesc. Instrum. Syst.* **2**(1), 011005 (2015).
21. F. Zernike, "Diffraction theory of the knife-edge test and its improved form, the phase-contrast method," *MNRAS*, **94**, 377 (1934).
22. J. W. Goodman, *Introduction to Fourier Optics*, 2nd ed., pp. 220–222, McGraw-Hill, New York (1996).
23. M. Born and E. Wolf, "Electromagnetic theory of propagation, interference and diffraction of light," in *Principles of Optics*, 7th ed., Cambridge University Press, Cambridge, Massachusetts (1999).
24. M. N'Diaye et al., "Calibration of quasi-static aberrations in exoplanet direct-imaging instruments with a Zernike phase-mask sensor," *Astron. Astrophys.* **555**, A94 (2013).
25. M. W. McElwain et al., "PISCES: An Integral Field Spectrograph to advance high contrast imaging technologies," *Proc SPIE* **8864**, 88641O (2013).
26. E. Sidick et al., "Studies of the effects of actuator errors on the HCIT/PIAA contrast performance," *Proc. SPIE* **7731**, 77314T (2010).
27. O. Guyon, B. Kern, and F. Martinache, "Phase-induced amplitude apodization (PIAA) technology development milestone #2: instrument tip-tilt control demonstration at sub-milliarcsecond levels," http://exep.jpl.nasa.gov/files/exep/PIAAmilestone2_final120821.pdf (29 February 2016).
28. R. Soummer et al., "Fast computation of Lyot-style coronagraph propagation," *Opt. Express* **15**(24), (2007).
29. A. Toorian et al., "Flight qualification and performance testing of SIM precision optical mechanisms," *Proc. SPIE* **7734**, 77341O (2010).
30. B. Kern, "Impact of WFIRST-AFTA line-of-sight jitter distributions on phase-induced amplitude apodization complex mask coronagraph science yield," *J. Astron. Telesc. Instrum. Syst.* **2**(1), 011014 (2015).
31. E. Sidick, S. A. Basinger, and D. C. Redding, "An improved wavefront control algorithm for large space telescopes," *Proc. SPIE* **7015**, 70154P (2008).

Fang Shi is a senior optical engineer at Jet Propulsion Laboratory. He received his BS degree in optical engineering from Zhejiang University in 1984, MS degree in optical science from the Institute of Optics and Electronics, Chinese Academy of Sciences in 1987, and PhD in astronomy from the University of Chicago in 1999. His research interests include wavefront sensing and control and coronagraph instrumentation. He leads the WFIRST coronagraph LOWFS/C task at JPL.

Kunjithapatham Balasubramanian is a senior optical engineer at the Jet Propulsion Laboratory, California Institute of Technology. With a PhD in optical sciences from the University of Arizona, he conducts research on optical materials, thin films, and micro/nanostructured optical devices. He leads the development of exoplanet coronagraph masks for testbeds at JPL, Princeton University, and NASA ARC. He is also engaged in the development of coatings for spectrometers and advanced UVOIR telescope optics.

Keith Patterson received his BS degree in mechanical and aerospace engineering from Rensselaer Polytechnic in 2007. He supported the MSL rover actuator development work in 2006 to 2008, and he also created configuration concepts for TeamX studies. He received his PhD from Caltech in 2013 in aeronautics, where he worked on lightweight deformable mirror technology. Currently, he is involved with exoplanet projects including the AFTA coronagraph and star shade.

Ilya Poberezhskiy received his BS, MS, and PhD degrees in electrical engineering from University of California, Los Angeles, in 1999, 2001, and 2004, respectively. Since then, he has worked at Caltech Jet Propulsion Laboratory in Pasadena, California, in the areas of optical metrology, high-reliability lasers, optical system integration and testing, and high-contrast imaging. Since 2014, he has managed the technology development testbeds for the WFIRST coronagraph instrument.

Joel Shields is a senior member of the Guidance and Control Analysis Group at the Jet Propulsion Laboratory. He received his BS degree in applied mechanics from UC San Diego in 1990 and his MS and PhD degrees in control systems from UC Berkeley in 1993 and 1997, respectively. Upon graduation, he worked as a consultant before joining JPL. At JPL he has worked on formation flying, interferometry, optical communications, cubesats, and coronagraphy.

Erkin Sidick received his BS degree in EE from Xinjiang University, China, in 1983, his MS degree in physics from CSUN in 1990, and his PhD in EE from UC Davis in 1995, both in the USA. He joined

JPL in 2004 and has worked on a variety of projects related to space telescopes, conducting optical modeling and simulations in the areas of wavefront sensing and control as well as integrated modeling.

J. Kent Wallace is a senior member of the technical staff at the Jet Propulsion Laboratory. He received his BS degree in physics from Rose-Hulman Institute of Technology in 1988 and his MS degree in optics from the University of Rochester in 1992. His research activities are centered around exoplanet detection and include wavefront sensing and control, adaptive optics, interfereometry, and radial velocity.

Xu Wang is a senior member of the technical staff at Jet Propulsion Laboratory. He has been working in the photonics fields for many years and has over 45 scientific publications. Currently, he is working on the development of wavefront sensing and control technology for various large telescope projects. He received his PhD in electrical engineering from the California Institute of Technology.

Biographies for the other authors are not available.